Improved Ocean–Fog Monitoring Using Himawari-8 Geostationary Satellite Data Based on Machine Learning With SHAP-Based Model Interpretation

Seongmun Sim and Jungho Im, *Member, IEEE*

***Abstract*—Ocean–fog is a type of fog that forms over the ocean and has a visibility of less than 1 km. Ocean–fog frequently causes incidents over oceanic and coastal regions; ocean–fog detection is required regardless of the time of day. Ocean–fog has distinct thermo-optical properties, and spatially and temporally extensive ocean–fog detection methods based on geostationary satellites are typically employed. Infrared (IR) channels of Himawari-8 were used to construct three machine-learning models for the continuous detection of ocean–fog. In contrast, visible channels are valid only during the daytime. As control models, we used fog products from the National Meteorological Satellite Center (NMSC) and machine-learning models trained by adding a visible channel. The extreme gradient boosting model utilizing IR channels corrected ocean–fog perfectly day and night, with the highest *F*1 score of 97.93% and a proportion correct (PC) of 98.59% throughout the day. In contrast, the NMSC product had a probability of detection of 87.14%, an *F*1 score of 93.13%, and a PC of 71.9%. As demonstrated by the qualitative evaluation, the NMSC product overestimates clouds over small and coarsely textured ocean–fog regions. In contrast, the proposed model distinguishes between ocean–fog, clear skies, and clouds at the pixel scale. The Shapley additive explanation analysis demonstrated that the difference between channels 14 and 7 was very useful for ocean–fog detection at night, and its extremely low values contributed significantly to distinguishing nonfog during the daytime. Channel 15, affected by water vapor absorption, contributed most to ocean–fog detection among atmospheric window channels. The research findings can be used to improve operational ocean–fog detection and forecasting.**

***Index Terms*—Himawari-8, machine learning, ocean–fog, Shapley additive explanation (SHAP), whole-day, extreme gradient boosting (XGB).**

I. Introduction

FOG is a near-surface cloud composed of small water droplets (1–50 μm) that strongly scatter visible light [1]. A phenomenon in which horizontal visibility falls below 1 km is defined as fog, which frequently causes traffic problems [1], [2], [3], [4]. Low visibility is even more dangerous when sailing because it takes longer to steer and brake than other ground vehicles [5], [6]. Even though many marine activities are susceptible to poor visibility, ocean–fog monitoring based on weather stations and video surveillance facilities is located on coastal land or ports, whereas the entire ocean is a potentially dangerous ocean–fog area [7], [8], [9], [10]. Therefore, monitoring ocean–fog over vast oceanic areas not limited to the coastal regions is essential.

Numerical weather prediction is widely used to estimate and forecast weather conditions by simulating atmospheric interactions and producing maps of atmospheric conditions, including ocean–fog over a large area. Although relative humidity can theoretically be used to estimate ocean–fog, the conditions that favor ocean–fog are intricately linked from microscale ($\sim$10-7 m) aerosol particle concentrations to synoptic-scale ($\sim$106 m) airmass behavior, resulting in poor modeling performance [11]. Numerous studies have proposed methods to improve multiscale modulation by combining multiple models, such as the Lagrangian cloud model, with large-eddy simulations; however, these approaches are insufficient to produce definitive ocean–fog simulations [12].

In addition to numerical simulations, satellite remote sensing provides data over vast areas. Owing to its unique thermo-optical properties, ocean–fog can be detected using meteorological satellite sensors [13], [14]. In addition, because ocean–fog monitoring necessitates frequent data acquisition, geostationary meteorological satellites with high temporal resolution (e.g., 10 min) may be an attractive option. As small water particles largely comprise ocean–fog-scattered short-wavelength light, visible channels of satellite sensors are frequently used to identify ocean–fog during the daytime [2], [14], [15], [16]. However, the spectral characteristics of visible wavelengths on ocean–fog are not easily distinguished from those on clouds. Spatial texture information has been used to distinguish ocean–fog from clouds because vertical mixing is more dynamic in clouds than in ocean–fog, resulting in a smoother top surface texture of ocean–fog [16], [17], [18]. The standard deviation of pixel values within the surrounding area (e.g., 3×3 and 5×5) was used to indicate the spatial texture of ocean–fog; however, it can result in underestimation at the edge of ocean–fog or a jumbled area of ocean–fog with clouds where the texture is relatively rough [13]. Ocean–fog and clouds can be distinguished by the thermal properties of ocean–fog even during the daytime, and thermal IR

Manuscript received 20 June 2023; revised 29 July 2023; accepted 20 August 2023. Date of publication 23 August 2023; date of current version 1 September 2023. This work was supported in part by the Korea Institute of Marine Science and Technology Promotion funded by the Ministry of Oceans and Fisheries, Korea under Grant 20180456 and Grant RS-2023-00256330; in part by the Development of Risk Managing Technology Tackling Ocean and Fisheries Crisis Around Korean Peninsula by Kuroshio Current under Grant RS-2023-00238486; and in part by the Monitoring Environmental and Ecological Changes in Dynamic Coasts and Estuaries of the Korean Four Major Rivers. *(Corresponding author: Jungho Im.)*

The authors are with the Department of Civil, Urban, Earth, and Environmental Engineering, Ulsan National Institute of Science and Technology, Ulsan 44919, South Korea (e-mail: smsim@unist.ac.kr; ersgis@unist.ac.kr).

Digital Object Identifier 10.1109/JSTARS.2023.3308041

(TIR) and brightness temperature differences (BTDs) between TIR and short-wavelength IR (SWIR) channels with their texture information have been used to detect ocean–fog [18]. At night, ocean–fog detection is typically implemented using the thermal properties of ocean–fog because visible channels are unavailable [17], [19], [20]. Even though an SWIR channel indicates mixed information on solar reflectance and surface emissions during the daytime, it can be used as a remarkable channel for ocean–fog detection by differentiating it from TIR channels at night because it implies only surface emissions during the nighttime [17], [19].

The National Meteorological Satellite Center (NMSC) of the Korean Meteorological Administration and the National Oceanic and Atmospheric Administration of the USA operate near real-time ocean–fog detection in Korea and the USA, respectively. They detected ocean–fog throughout the day by utilizing successively connected models with various temporal windows (i.e., daytime, nighttime, and dawn/dusk models). Although each model was properly calibrated for its target temporal window, spatiotemporal discontinuities in the detected ocean–fog were observed during the model transitions. Discontinuous ocean–fog detection negatively affects traffic control and forecasters; thus, spatiotemporally continuous ocean–fog detection is required.

A temporally integrated model based on infrared (IR) channels is a suitable solution for ocean–fog monitoring. However, although IR channels can discriminate ocean–fog from other classes, such as clouds and clear skies, for both day and night, ocean–fog characteristics vary with time [17], [18]. Thus, using solar position information in advanced empirical models may improve the spatiotemporal continuity of ocean–fog. In this article, machine-learning approaches (random forest, RF; extreme gradient boost, XGB; and logistic regression, LR), which have been demonstrated to be effective for detecting meteorological features under complex conditions [21], [22], [23], [24], [25], [26], were utilized to detect ocean–fog with various characteristics. However, nonfog phenomena (e.g., clear skies and clouds) were trained to mitigate the confusion between ocean–fog and other phenomena. Two schemes were examined: one scheme using only IR channels (IRO) that can be applied regardless of the time of day, and another scheme employing both IR and visible channels (VIS). The models with the two schemes were compared with the NMSC product. This article used Himawari-8 data to detect ocean–fog between China and the Korean Peninsula over the Yellow Sea. The Shapley additive explanation (SHAP) approach was employed to interpret the contributions and interactions of the input variables in the models.

II. Study Area and Data

A. Study Area and Data

The study area was the Yellow Sea (33–40°N, 119–128°E) in Northeast Asia, which is surrounded by the Korean Peninsula and China and features active fishing and maritime trade (see Fig. 1). The Yellow Sea is characterized by a shallow bathymetry, leading to the formation of stratified cold-water masses beneath the seasonal thermocline layer [27]. During the warm season, strong vertical mixing results in cool sea surface temperature (SST) [27], [28]. Advection fog, the most common type of ocean–fog, forms when warm and humid air masses interact with a cold surface; ocean–fog is prevalent in this region from May to October during the summer season [7], [29].

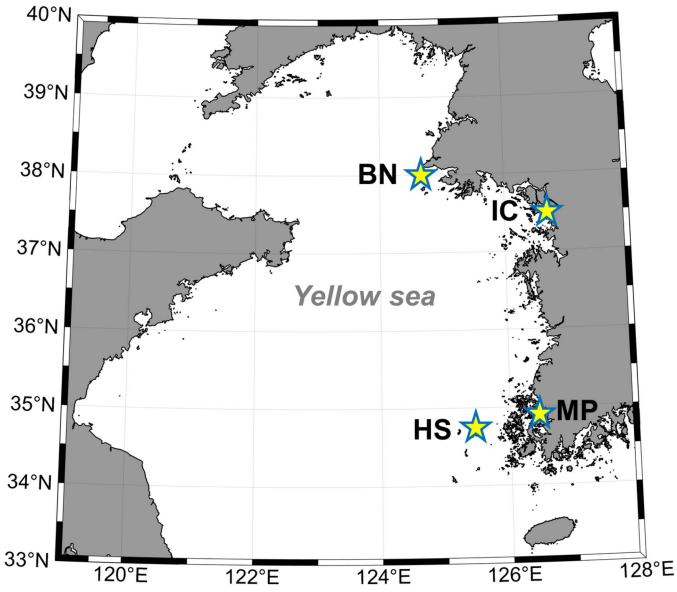

Fig. 1. Study area with the location of automated surface observing system stations that measure visibility located in the coast or islands. Four stations are Baenyeongdo (BN), Heuksando (HS), Incheon (IC), and Mokpo (MP).

B. Ocean–Fog Reference Data

To construct an accurate ocean–fog detection model, nonfog classes, such as clear skies and clouds, should be specified. The Automated Surface Observing System (ASOS) and Cloud-Aerosol Lidar and Infrared Pathfinder Satellite Observation (CALIPSO) were used as reliable reference data sources for collecting samples for three classes (ocean–fog, clear skies, and clouds) [13], [14], [17], [19], [20]. The ASOS field measurement system provides hourly meteorological and weather information, including visibility, to determine ocean–fog [16], [30], [31]. South Korea has 102 ASOS stations and autonomous visibility measurements have been available since 2017 [32]; therefore, data from 2017 to 2021 were utilized for this article. Baenyeongdo (BN) at 37.97°N, 124.71°E, Heuksando (HS) at 34.69°N, 125.45°E, Incheon (IC) at 37.48°N, 126.62°E, and Mokpo (MP) at 34.82°N, 126.38°E were chosen as reference ASOS stations for this article because they are located on the coast or islands where ocean–fog frequently occurs (see Fig. 1 and Table I). Although visibility is automatically measured, human experts still measure clouds subjectively. Therefore, additional quality checks are necessary to utilize the cloud data collected from ASOS stations.

CALIPSO, launched in 2007, is a polar-orbiting laser altimetry satellite equipped with cloud-aerosol lidar with an orthogonal polarization sensor. Using two distinct active beams (532 and 1064 nm) with a 5-km swath and 5-km intervals along

TABLE I
NUMBER OF COLLECTED REFERENCE CASES OF THREE CLASSES FOR EACH DATA SOURCE FROM 2015 TO 2021

		Daytime			Nighttime		
		Ocean–fog	Clear skies	Clouds	Ocean–fog	Clear skies	Clouds
ASOS	Baenyeongdo (BN)	75 (9)	32 (0)	189 (30)	294 (26)	177 (0)	19 (3)
	Heulksando (HS)	55 (8)	11 (0)	177 (31)	122 (18)	109 (0)	31 (6)
	Incheon (IC)	5 (0)	10 (0)	179 (17)	40 (5)	60 (0)	23 (1)
	Mokpo (MP)	2 (0)	12 (0)	133 (25)	3 (2)	43 (0)	25 (1)
CALIPSO		17 (4)	145 (24)	280 (53)	34 (3)	146 (33)	234 (58)
Total		154 (21)	210 (24)	958 (156)	493 (54)	535 (33)	332 (69)

The number of cases in 2021 used for Hindcast evaluation is in parentheses.

the track, CALIPSO investigates the particle components of the atmospheric column, including aerosols and clouds, with 545 vertical layers at time intervals of less than 1 min [33]. Information about the particle composition was converted into the presence of clouds and aerosols and provided as a vertical feature mask (VFM), a level-2 product. Owing to the absence of ocean–fog information in the VFM product, an algorithm proposed by Wu et al. [3] was used to obtain ocean–fog reference data. This algorithm identifies ocean–fog layers by detecting abnormally high ocean surfaces or surface-attaching clouds and implementing additional quality control (QC) rules using the attenuated backscatter of a 532 nm beam. Raw VFM data with an additional quality check were utilized for the clear-sky and cloud layers, and homogeneous cases were selected across the CALIPSO swath (5 km). This article utilized CALIPSO data collected between April 2015 and December 2021, matching the availability of Himawari-8 satellite imagery as the input data. Because the ocean–fog detection system must guarantee performance for newly acquired cases when operational, cases from 2021 were used for the hindcast evaluation. In contrast, cases from 2015 to 2020 were used for calibration. Table I summarizes the number of reference cases by class, data source, and model.

C. Himawari-8

Himawari-8 is a meteorological satellite in a geostationary orbit administered by the Japan Meteorological Agency. Himawari-8 is equipped with an advanced Himawari Imager and a multispectral sensor with three visible, three near-IR, and ten IR wavelength channels [34]. To distinguish ocean–fog from other classes—clear skies and clouds—well-known ocean–fog and cloud-sensitive channels (Ch02, Ch07, and Ch14), high-, mid-, and low-level water vapor absorption channels (Ch08, Ch09, and Ch10), and dirty window channels (Ch11 and Ch15) were considered as input features, as marine atmospheric conditions typically exhibit different characteristics on these channels (see Table II) [14], [17], [20], [35], [36], [37]. The BTDs between the IR channels and the solar zenith angle (SOZ) were used as input features to enhance and clarify the signals of marine atmospheric conditions over time (see Table II) [35], [36], [37], [38].

III. METHODOLOGY

This article proposes whole-day composite models for ocean–fog detection based on machine-learning techniques and Himawari-8 data (see Fig. 2). To construct and evaluate the models, samples of target classes (i.e., ocean–fog, clear skies, and clouds) were collected from a homogeneous region identified through K-means clustering. Uncertainties can be introduced even if a homogeneous area spatially matches a reference point; therefore, QC procedures (e.g., target class agreement test, shape filtering, potential cloud-intruding filtering, and theoretical filtering) are implemented. As two types of schemes (i.e., IRO and VIS) were examined independently, machine-learning models (i.e., RF, XGB, and LR) were constructed after the optimization of the target class composition and hyperparameter tuning using the calibration set (2015–2020), and evaluated using the hindcast validation set (2021). The SHAP method was adopted to interpret the machine-learning models, focusing on the contribution and interactions of the input features, followed by spatiotemporal evaluations.

A. Sample Extraction

Because ocean–fog reference data are typically collected as points (e.g., specific ASOS stations or CALIPSO shots), previous articles have usually increased their sample size through

TABLE II
SUMMARY OF INPUT VARIABLES FROM HIMAWARI-8 SATELLITE DATA FOR DEVELOPING OCEAN–FOG DETECTION MODELS IN THIS ARTICLE

Variable name	Description	Characteristics
Ch02	Albedo of 0.50–0.52 μm channel (unitless)	Sensitive to the feature reflectance
Ch07	BT* of 3.74–3.96 μm channel (Kelvin)	Surface emission. Solar reflectance in the daytime
Ch08	BT of 5.77–6.6 μm channel (Kelvin)	High-level water vapor absorption
Ch09	BT of 6.75–7.15 μm channel (Kelvin)	Mid-level water vapor absorption
Ch10	BT of 7.26–7.43 μm channel (Kelvin)	Low-level water vapor absorption
Ch11	BT of 8.44–8.76 μm channel (Kelvin)	Atmospheric window/ water vapor absorption
Ch14	BT of 11.1–11.3 μm channel (Kelvin)	Classical atmospheric window
Ch15	BT of 12.2–12.5 μm channel (Kelvin)	Atmospheric window/ water vapor absorption
†BTD1007	BTD between Ch10 and Ch07 (Kelvin)	Emphasizing low-level clouds at night
BTD1107	BTD between Ch11 and Ch07 (Kelvin)	Emphasizing low-level water clouds at night
BTD1407	BTD between Ch14 and Ch07 (Kelvin)	Emphasizing low-level clouds at night
BTD1411	BTD between Ch14 and Ch11 (Kelvin)	Emphasizing warm cloud
SOZ	Solar zenith angle (degree)	Implying time information

BT: Brightness temperature
†BTD: Brightness temperature difference

spatial oversampling, such as collocation with human-inspected ocean–fog patches [14], [16] or the use of neighborhood pixels [13], [17]. However, although human inspection of ocean–fog patches can provide as many ocean–fog samples (pixels) as possible, they require considerable human resources. In addition, they are only available under ideal conditions (i.e., daytime, no cloud contamination, and large expanded ocean-fog). Merging nearby pixels, on the other hand, works without human resources and specific conditions but produces a much smaller number of pixels (e.g., 9-pixel or 25-pixel) regardless of how large an ocean–fog patch is, and it has spatial autocorrelation issues.

Unsupervised image segmentation is a promising approach for acquiring spatially expanded potential ocean–fog patches [39], [40]. It divides the images into several mutually exclusive segments with similar characteristics. This article used the K-means clustering method to obtain spatially expanded ocean–fog patches [37], [38], [39], [40], [41], [42], [43]. The K-means clustering method divides the input data into K groups with similar properties by minimizing the sum of the squared distances between the data points and centroids of the clusters, where each data point is assigned to the cluster with the nearest centroid [44], [45]. Images of Ch02, Ch14, BTD1107, BTD1407, and BTD1514, which have relatively distinct value ranges for the target classes (i.e., ocean–fog, clear skies, and clouds), were used as inputs for K-means clustering. At night, all pixel values of the visible Ch02 images were filled with zeros so that they could not be used for clustering. As the k value increased, the segments' average size decreased while each segment's purity increased; consequently, a relatively high K value of 25 was chosen based on numerous empirical experiments to extract pure sample data.

An additional QC was implemented due to the spatial scale difference between the point reference and grid satellite data. For instance, a cluster may contain two or more reference classes or a cloud edge above an ocean–fog cluster may be assigned. Clusters containing multiple classes were easily eliminated, but ocean–fog clusters assigned to cloud edges required a more intricate correction process owing to their high transparency. Edge segments typically have an irregular shape, thin or long, and can therefore be filtered using a metric called the fractal dimension index (FRAC) (1) [46], [47], [48]. FRAC is a metric used to quantify the shape irregularity of an object based on its perimeter and area and ranges from 1 to 2. A shape with an FRAC close to 1 is considered simple, whereas a shape with an FRAC close to 2 is considered extremely convoluted [48]. Through empirical testing, a QC procedure was added to the segments of the three classes—ocean–fog, clear skies, and clouds—to filter

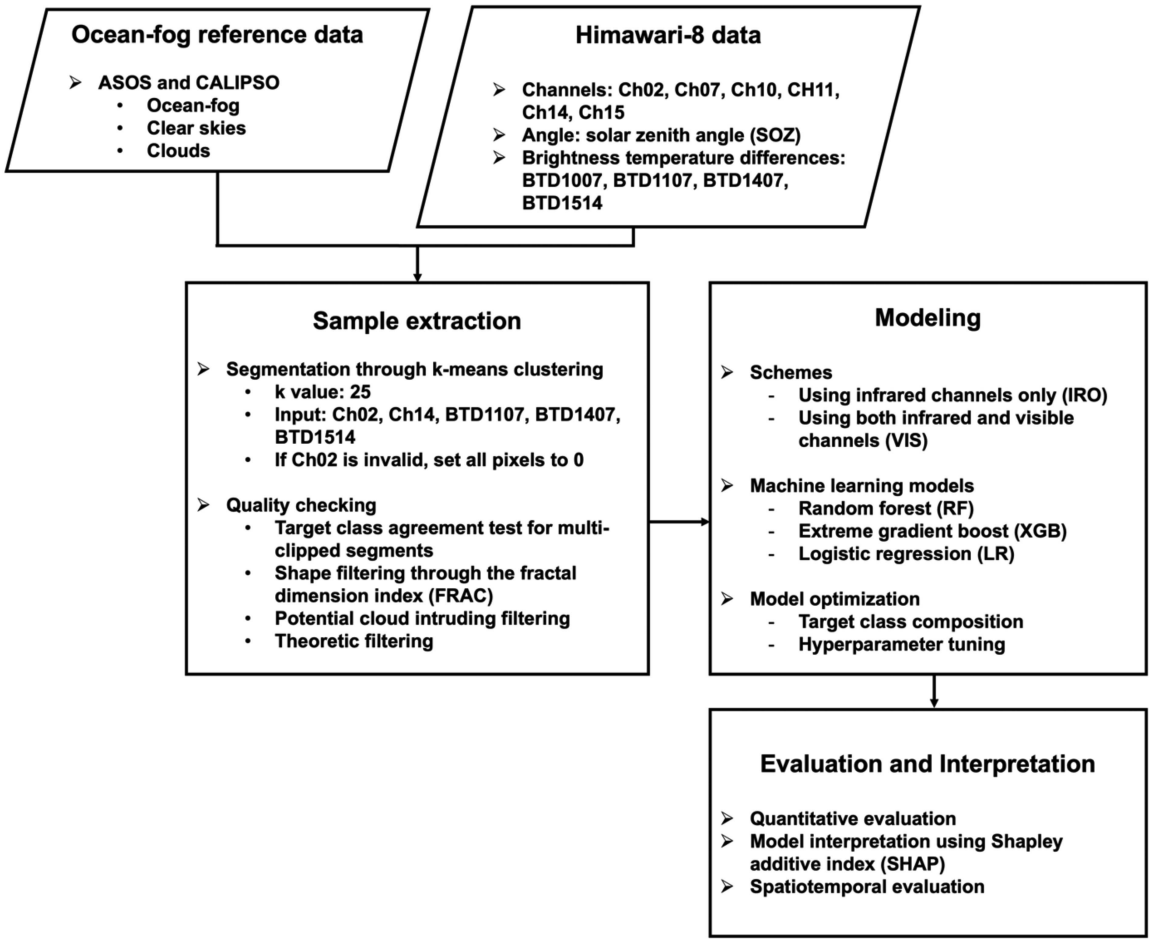

Fig. 2. Process flow proposed in this article.

out those with an FRAC value >1.4 and 1.6, respectively

$$\text{FRAC} = \frac{2 \times \log\left(0.25 \times \text{perimeter}\right)}{\log\left(\text{area}\right)}. \tag{1}$$

When matching ocean–fog reference data with the Himawari-8 images, temporal buffers (i.e., a time difference of less than 5 min) were applied to the CALIPSO data. Even a time difference of less than 5 min can cause mismatching between the reference data and Himawari-8 images owing to migrating clouds; therefore, spatial buffers were used to eliminate the possibility of cloud intrusion: only reliable when reference points were located more than 2 or 4 km away from the edge of segments with time differences of less than 3 min or more, respectively. Finally, several physical quality-checking criteria were applied to each segment to guarantee the reliability of the input data: Ch14 $\geq$ 273.15 K and Ch02 $\geq$ 0.1 for daytime ocean-fog and Ch14 $\geq$ 273.15 K for nighttime ocean-fog; Ch14 $\geq$ 273.15 K and Ch02 $\leq$ 0.15 for daytime clear skies and Ch14 $\geq$ 273.15 K for nighttime clear skies; Ch02 $\geq$ 0.1 for daytime clouds, Ch07 $<$ 284 K for summer nighttime clouds, and Ch07 $<$ 270 K for winter nighttime clouds (Ch02 related rules are only executed when the visible channel is valid). These criteria are based on the theoretically valid range of each marine atmospheric condition, except for cloud-related criteria, which are enhanced by human inspection of cloud reports [49], [50].

B. Modeling

This article evaluated two IRO and VIS schemes for ocean–fog detection. The IRO scheme was designed to detect ocean–fog throughout the day using only IR channels. In contrast, the VIS scheme was designed to detect ocean–fog during the daytime using IR channels with a visible channel. Three distinct machine-learning algorithms were used for each scheme to detect ocean–fog: RF, XGB, and LR inspired by bagging, boosting, and logarithmically adapted regression, respectively [51], [52], [53]. The RF model is an ensemble of classification and regression trees (CART) that generates decisions through recursive binary divisions [54], [55].

Given that the CART is susceptible to overfitting based on training samples, random subsets of training samples and variables were applied to each CART to produce multiple independent trees in the RF. The XGB is also composed of CARTs; however, the calibration process differs from that of the RF model. To achieve high performance, XGB recursively updates a model with the incremental weighting of misclassified sample components [53]. The RF and XGB models are rule-based and

TABLE III
INPUT VARIABLES AND TRAINING PARAMETERS OF MACHINE LEARNING MODELS USED IN THIS ARTICLE

	Infrared channel only (IRO) scheme			Infrared with a visible channel (VIS) scheme		
	Random forest (IRO_RF)	Extreme gradient boosting (IRO_XGB)	Logistic regression (IRO_LR)	Random forest (VIS_RF)	Extreme gradient boosting (VIS_XGB)	Logistic regression (VIS_LR)
Input variable	Ch07, Ch08, Ch09, Ch10, Ch11, Ch14, Ch15, BTD1007, BTD1107, BTD1407, BTD1411, and SOZ			Ch02, Ch07, Ch08, Ch09, Ch10, Ch11, Ch14, Ch15, BTD1007, BTD1107, BTD1407, BTD1411, and SOZ		
Target class composition ratio	Ocean-fog: Clear skies: Clouds = 1.0: 1.0: 0.7			Ocean-fog: Clear skies: Clouds = 1.0: 1.0: 1.0		
Model parameter	n_estimators = 500 max_depth = 10 min_samples_leaf = 14 min_samples_split = 12	n_estimators = 500 max_depth = 10 colsample_bytree = 0.9 min_child_weight = 2 subsample = 0.8 learning_rate = 0.1 min_split_loss = 0.05 reg_alpha = 0.01 objective = 'multi:softprob' eval_metric = 'mlogloss'	max_iter =1000 C = 1 penalty = 'l2' multi_class = 'multinomial'	n_estimators = 500 max_depth = 8 min_samples_leaf = 3 min_samples_split = 14	n_estimators = 500 max_depth = 10 colsample_bytree = 0.8 min_child_weight = 2 subsample = 0.8 learning_rate = 0.1 min_split_loss = 0.05 reg_alpha = 0.01 objective = 'multi:softprob' eval_metric = 'mlogloss'	max_iter =1000 C = 0.01 penalty = 'l2' multi_class = 'multinomial'

TABLE IV
CONTINGENCY TABLE OF THREE CLASSES FOR QUANTITATIVE EVALUATION OF THE PROPOSED OCEAN–FOG DETECTION MODELS

		Observation			
		Ocean–fog	Clear	Cloud	Sum
Prediction	Ocean–fog	N_{ff}	N_{rf}	N_{df}	S_{pred_f}
	Clear	N_{fr}	N_{rr}	N_{dr}	S_{pred_r}
	Cloud	N_{fd}	N_{rd}	N_{dd}	S_{pred_d}
	Sum	S_{org_f}	S_{org_r}	S_{org_d}	S_{all}

make decisions based on threshold-based classification nodes, whereas the LR model relies on regression. LR is a sophisticated form of linear regression-based classification that uses a logistic function to calculate the probability of a target variable class. Although LR has a simpler structure than tree-based models, its log-transformed regression forms enable the incorporation of nonlinear relationships between input variables and targets [56].

The collected samples were divided into a calibration set (from 2015 to 2020) and a hindcast validation set (samples from 2021). As the sample size varied greatly by class, it was further optimized to avoid biased modeling results caused by imbalanced training data [23]. Based on the performance of the 10-fold cross-validation, the optimum sample size ratio by class (i.e., ocean–fog, clear skies, and clouds) was determined to be 1.0:1.0:0.7 for the IRO scheme and 1.0:1.0:1.0, for the VIS scheme, with 96 600 and 20 600 ocean–fog samples for the IRO and VIS schemes, respectively (see Table III). To ensure a fair evaluation of the hindcasts, the case numbers of each nonfog class (i.e., clear skies and clouds) were matched to those of ocean–fog. A grid search was used to optimize the hyperparameters of the machine-learning models (see Table III) [57]. The maximum depth of a tree (max_depth), the minimum number of samples required to be at a leaf node (min_sample_leaf), the minimum number of samples required to split an internal node (min_samples_split), and the number of trees (*n*_estimators) were optimized for RF; the step size shrinkage used in the update to prevents overfitting (learning rate), *n*_estimators, max_depth, the minimum sum of instance weight needed in a child (min_child_weight), the subsample

TABLE V
HINDCAST CLASSIFICATION RESULTS OF MACHINE-LEARNING MODELS AND AMI PRODUCTS

		IR-only scheme (IRO)			With visible scheme (VIS)			Control
		RF	XGB	LR	RF	XGB	LR	NMSC
Day	POD	100	100	70	100	100	100	90
	FAR_r	0	0	6.67	0	0	0	0
	FAR_d	4.76	0	0	4.76	4.76	4.76	0
	F1	97.56	100	80	97.56	97.56	97.56	94.74
	PC	98.33	100	88.33	98.33	98.33	98.33	96.67
Night	POD	96.08	100	78.43				86
	FAR_r	0	5.56	29.82				0
	FAR_d	0	0	0				0
	F1	98	97.14	74.08				92.47
	PC	98.69	98.04	81.05				62
Whole-day	POD	97.18	100	76.06				87.14
	FAR_r	0	4.05	25				0
	FAR_d	1.43	0	0				0
	F1	97.87	97.93	75.53				93.13
	PC	98.59	98.59	83.1				71.9

Hindcast samples (2021) are independent of the training samples (2015–2020) used to develop the machine-learning-based models. All the units of indices are converted to the range from 0% to 100%.

ratio of the training instances (subsample), the subsample ratio of columns when constructing each tree, the L1 regularization term on weights (reg_alpha), and the minimum loss reduction required to make a further partition on a leaf node of the tree (min_split_loss) for XGB; and the inverse of regularization strength (C), and the specific the norm of the penalty (penalty), for LR [57].

C. Accuracy Assessment

The probability of detection (POD), false alarm ratio (FAR), $F1$-score, and proportion correct (PC) were used to evaluate the performance of the models in detecting ocean–fog. A case-by-case quantitative evaluation was conducted by assigning the most-classified class to each pixel set (see Table IV). POD is the proportion of ocean–fog cases classified as ocean–fog, representing the ocean–fog detection performance (3). FAR is the proportion of nonfog cases classified as ocean–fog, representing the false alarm rate for ocean–fog detection (3). For a more accurate analysis, the clear-sky and cloud cases of FAR were separated into FAR_r (4) and FAR_d (5), respectively. The $F1$-score is a harmonic mean of POD, and the complement of FAR represents a balanced performance for ocean–fog detection (6). PC is the proportion of corrected cases to the total number of cases, representing the overall performance of the classification (7) [58], [59]. The fog product of GeoKompsat-2A produced by NMSC (referred to as NMSC) [13] was compared to examine the operational feasibility of the models.

Because the reference data were collected at specific locations or times, such as ASOS stations or CALIPSO passing local time, a qualitative evaluation of the spatial distribution of ocean–fog was conducted using the CALIPSO VFM track as an example. In addition, the BN station was used to qualitatively assess the temporal continuity of the ocean–fog. Finally, all qualitative evaluations were compared to the control product (NMSC) and the inferred input variables Ch02 and Ch14

$$\mathrm{POD} = N_{\mathrm{ff}}/S_{\mathrm{org\_f}} \times 100\% \tag{2}$$

$$\mathrm{FAR} = N_{\mathrm{rf}}/S_{\mathrm{pred\_f}} \times 100\% \tag{3}$$

$$\mathrm{FAR\_}r = N_{\mathrm{rf}}/S_{\mathrm{pred\_}f} \times 100\% \tag{4}$$

$$\mathrm{FAR\_}d = N_{\mathrm{df}}/S_{\mathrm{pred\_}f} \times 100\% \tag{5}$$

$$F1\_\mathrm{score} = 2 \times \frac{\mathrm{POD} \times (100\% - \mathrm{FAR})}{\mathrm{POD} + (100\% - \mathrm{FAR})} \tag{6}$$

$$\mathrm{PC} = \left(N_{\mathrm{ff}} + N_{\mathrm{rr}} + N_{\mathrm{dd}}\right)/S_{\mathrm{all}} \times 100\%. \tag{7}$$

D. Model Interpretation

The SHAP was used to investigate the contribution and interactions of the input variables on the modeling results. The SHAP quantifies the contribution of input variables based on game theory to determine the effect of each input variable [60],

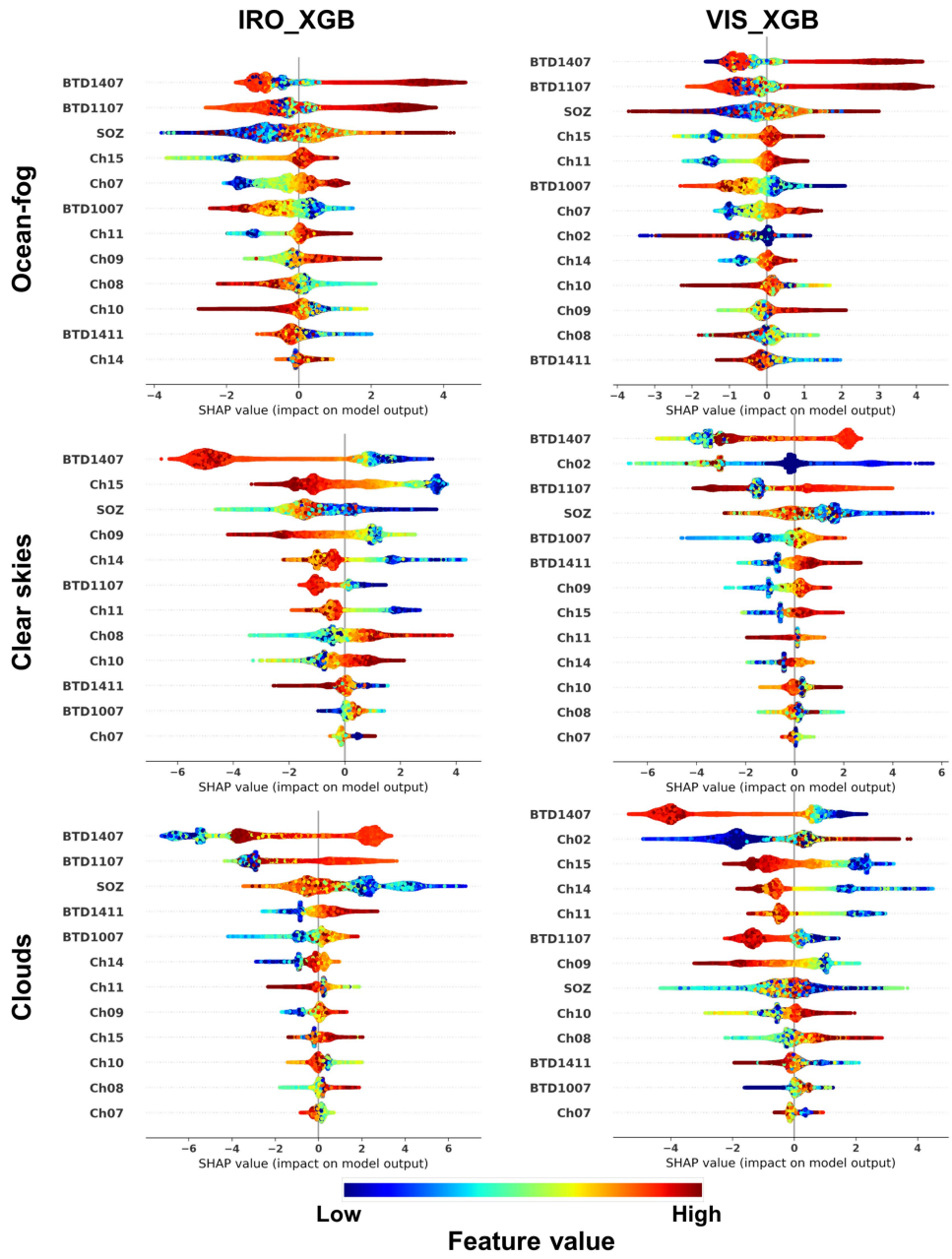

Fig. 3. SHAP value summary plots on XGB models in IRO and VIS scheme for target classes. The variables on the *y*-axis were arranged in descending order through the mean absolute SHAP values.

[61], [62]. Due to the complexity of the machine-learning model structure, SHAP considers the model as an aggregation of each input variable's value (z) and weight (φ). For example, the weight of input variable i can be interpreted as the contribution amount, which is estimated by calculating the difference in score between using and not using the variable (8) to determine the contribution (φi) of input variable i as follows:

$$\varphi_i = \sum_{S \subseteq N/\{i\}} \frac{|S|!\,(|N| - |S| - 1)!}{|N|!} \left(f\left(S \cup \{i\}\right) - f\left(S\right)\right) \tag{8}$$

where N denotes the entire set of variables, S denotes a subset of variables excluding i, the vertical bar brackets (|#|) denote the number of variables, and the factorial (!) denotes the number of possible combinations of provided variables. Equation (8) calculates the average score change ($f(x)$) for every possible combination of input variables. As this was a classification study, the score of the SHAP approach was defined as the classification probability for each target class. Not only is the mean absolute SHAP value used to determine the contribution rank of the input variables, but the dependence of variable contributions on the SOZ is also used to interpret the change in variable contribution as the SOZ changes, as the diurnal variation of the SOZ influences some variables.

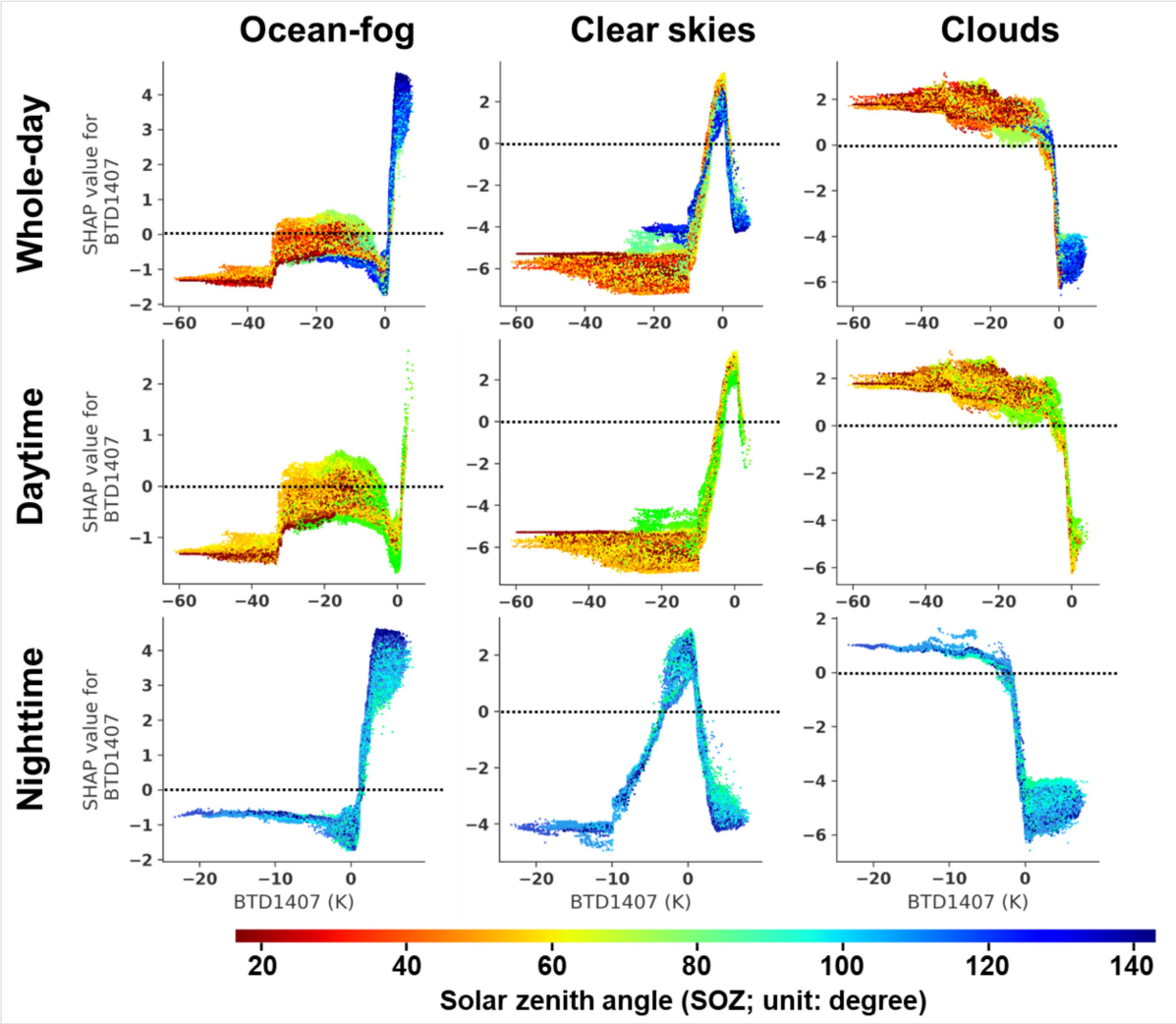

Fig. 4. Dependency plots of the brightness temperature difference between Ch14 and Ch07 by the solar zenith angle on extreme gradient boosting of infrared only used scheme in each temporal period. *X*-axis indicates values of input variables, the *y*-axis indicates SHAP values, and the color indicates the solar zenith angle.

IV. Results and Discussion

A. Quantitative Model Assessment

The hindcast validation results of the models are listed in Table V. During the daytime, except for IRO_LR and NMSC, all models accurately classified ocean–fog cases (POD of 100%). IRO_XGB and NMSC correctly classified daytime nonfog cases (FAR_r = 0% and FAR_d = 0%), whereas the IRO_RF and VIS models misclassified 4.76% of cloud cases as ocean–fog, and IRO_LR misclassified 6.67% of clear-sky cases as ocean–fog. Overall, IRO_XGB had an $F1$ of 100% but also a PC of 100%, indicating perfect classification across all classes, followed by the IRO_RF and VIS models with an $F1$ of 97.56%, and PC of 98.33%, NMSC with $F1$ of 94.74% and PC of 96.67%, and IRO_LR with $F1$ of 80% and PC of 88.33%, respectively.

During the nighttime, IRO_XGB had the best performance in detecting ocean—fog, with a POD of 100%, followed by IRO_RF with a POD of 96.08%, NMSC with a POD of 86%, and IRO_LR with a POD of 78.43%. However, in contrast to the daytime, some clear-sky cases were misclassified as ocean–fog (FAR_r of 5.56%) from IRO_XGB. In contrast, all nonfog cases were correctly classified as nonfog from IRO_RF and NMSC, and 29.82% of the clear-sky cases were misclassified as ocean–fog from IRO_LR. In terms of overall performance, IRO_RF exhibited the best results with an $F1$ of 98% and PC of 98.69%, followed by IRO_XGB with an $F1$ of 97.14% and PC of 98.04%, NMSC with an $F1$ of 92.47% and PC of 62%, and IRO_LR with an $F1$ of 74.08% and PC of 81.05%.

Even though IRO_XGB had the second-highest performance during nighttime, it correctly classified ocean–fog cases with no confusion with cloud cases, resulting in a POD of 100%, $F1$ of 97.93%, and PC of 98.59%, which was the highest performance of all models and products considering both day and night. However, although machine-learning models were designed to classify three types of marine atmospheric conditions (e.g., ocean–fog, clear skies, and clouds), the NMSC can only distinguish between ocean–fog and nonfog during the nighttime,

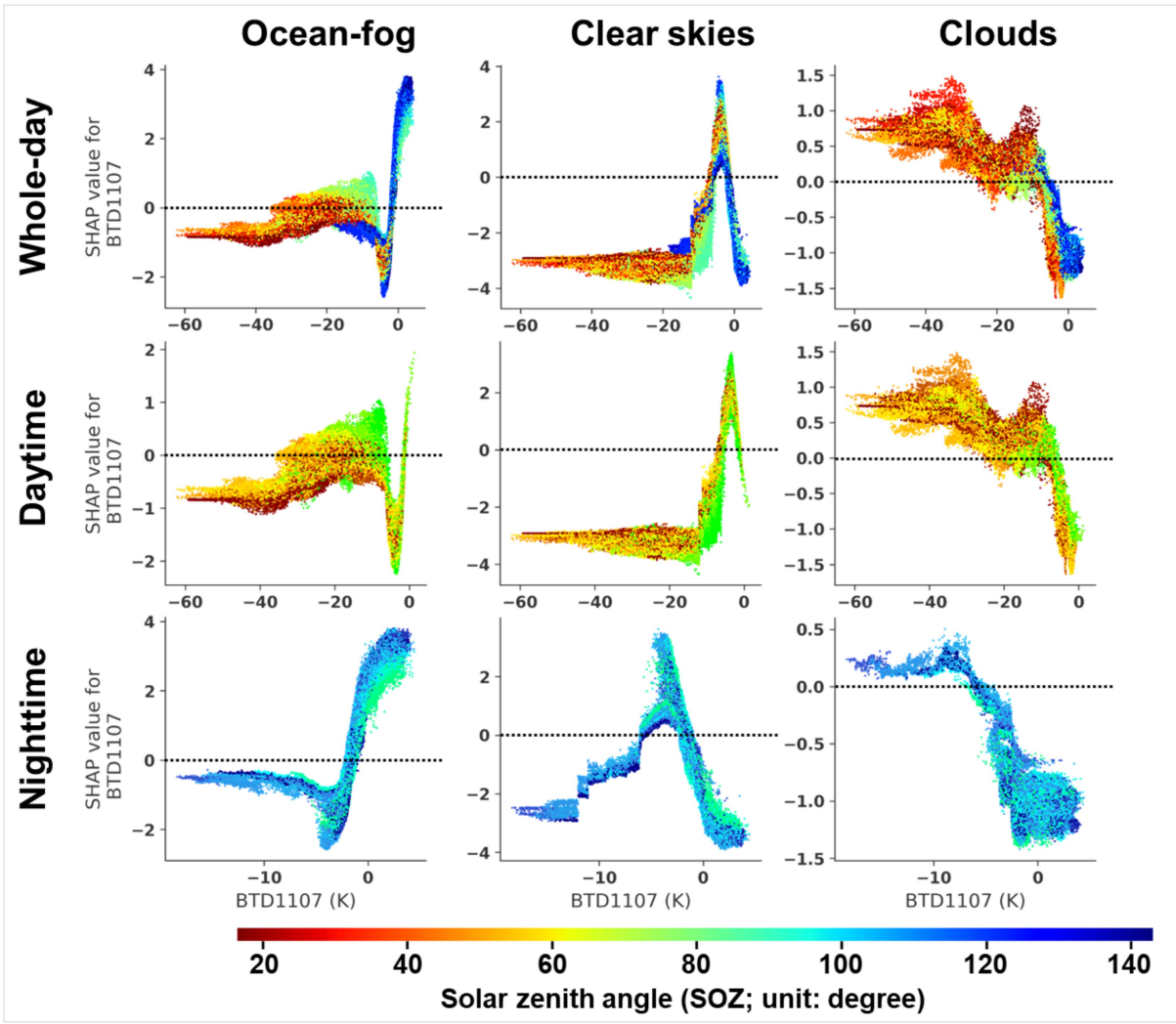

Fig. 5. Dependency plots of the brightness temperature difference between Ch11 and Ch07 by the solar zenith angle on extreme gradient boosting of infrared only used scheme in each temporal period. *X*-axis indicates values of input variables, the *y*-axis indicates SHAP values, and the color indicates the solar zenith angle.

resulting in poor performance on PC (62%) but high *F*1 (92.47%) during the nighttime [13].

Even though the VIS-based models were trained using daytime samples, IRO_XGB outperformed the VIS-based models regarding cloud discrimination, regardless of the time. The reason for this unexpected result is analyzed via SHAP analysis in Section IV-B. Furthermore, in contrast to the other machine-learning models, IRO_LR performed poorly for both daytime and nighttime, whereas VIS_LR performed comparably to the other models during the daytime. Furthermore, the regression-based LR calculation formula is ineffective when utilizing input variables with disorderly trends, such as Ch07, BTD1007, BTD1107, and BTD1407, whose day and night trends are radically dissimilar [63]. Finally, IRO_XGB was chosen as the best model for subsequent analysis, and VIS_XGB and NMSC were chosen as the daytime and whole-day control models, respectively, for further comparison.

B. Model Interpretation

Fig. 3 depicts summary plots of the SHAP values for each target class using IRO_XGB and VIS_XGB. Ch02 did not contribute significantly to ocean–fog classification (see Fig. 3 and Table V). However, it ranks second in variable contributions for classifying clear skies and clouds. Specifically, a lower Ch02 value significantly contributed negatively (<-2) to the noncloud detection. In contrast, most samples tilted toward an SHAP value of approximately zero for the clear sky classification.

Low Ch02 reflectance was used exclusively as an indicator of nonclouds for VIS_XGB (see Fig. 3), which could lead to confusion when low-reflectance cloud cases are provided, resulting in an atypically higher FAR_*d* for VIS_XGB than for IRO_XGB (see Table V). Because the values of Ch07-related variables vary significantly between day and night in ocean–fog and clouds, SOZ was anticipated to be utilized as a variable indicating diurnal variation in the IRO scheme. In the variable contribution

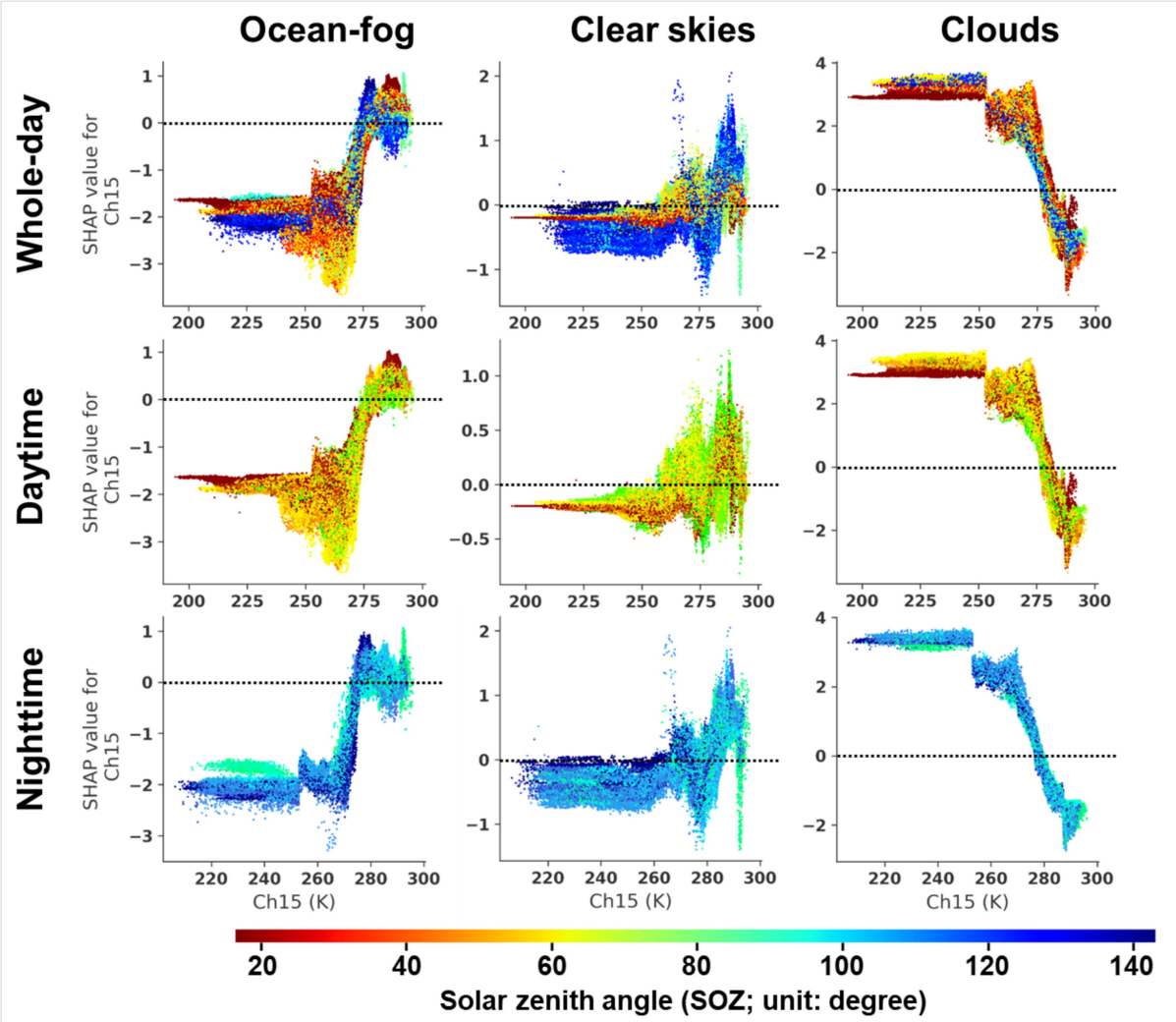

Fig. 6. Dependency plots of Ch15 by the solar zenith angle on extreme gradient boosting of infrared only used scheme in each temporal period. *X*-axis indicates values of input variables, the *y*-axis indicates SHAP values, and the color indicates the solar zenith angle.

summary, SOZ ranked third for all target classes of IRO_XGB; it also ranked third for ocean–fog classification of VIS_XGB with a noticeable pattern in SHAP values. Specifically, the high values of SOZ (night in IRO and day–night transition in the VIS scheme) contributed positively to the detection of ocean–fog, and the low values of SOZ (day in IRO and close to noon in the VIS scheme) contributed positively to the detection of clear skies and clouds. This SHAP distribution was deduced from the statistical tendency of ocean–fog, which is typically observed after sunset. Therefore, this variable indicates diurnal status; therefore, it was used as an independent variable in the analysis of the change in contribution due to diurnal variation in the dependence plot, despite its high contribution to the model. As the influence of Ch02 on VIS_XGB ocean–fog detection was minimal, dependency analysis by SOZ change was conducted only for IRO_XGB.

Among the input variables for ocean–fog detection contribution, BTD1407 and BTD1107 ranked first and second, respectively. Ch07, a component of BTD1407, is sensitive to solar radiation; thus, the relationship between BTD1407 and SOZ was analyzed using a dependency plot (see Fig 4). During the daytime (SOZ $\lesssim 80°$), BTD1407 values (from -35 to -5 K) contributed positively to the classification of ocean–fog samples, with some values having a negative contribution. Nonetheless, extremely low values ($\sim<-35$) contributed significantly to eliminating nonfog samples with SHAP lower than -1, while these values positively contributed to identifying clouds simultaneously. While ocean–fog and clouds have higher Ch07 reflectance than clear skies, ocean–fog and clear skies have high Ch14 BTs, and clouds have low Ch14 BTs. The reflectance of ocean–fog and clouds varies with their optical transparency and solar incidence angle; only very cold BT with high reflectance of clouds indicates extremely low values of BTD1407, which contributed significantly to distinguishing clouds, whereas the other positive contributing ranges overlapped with those for discriminating ocean–fog.

During the nighttime, values over 2 K of BTD1407 contributed to the SHAP up to a value of 5. At the same time, this

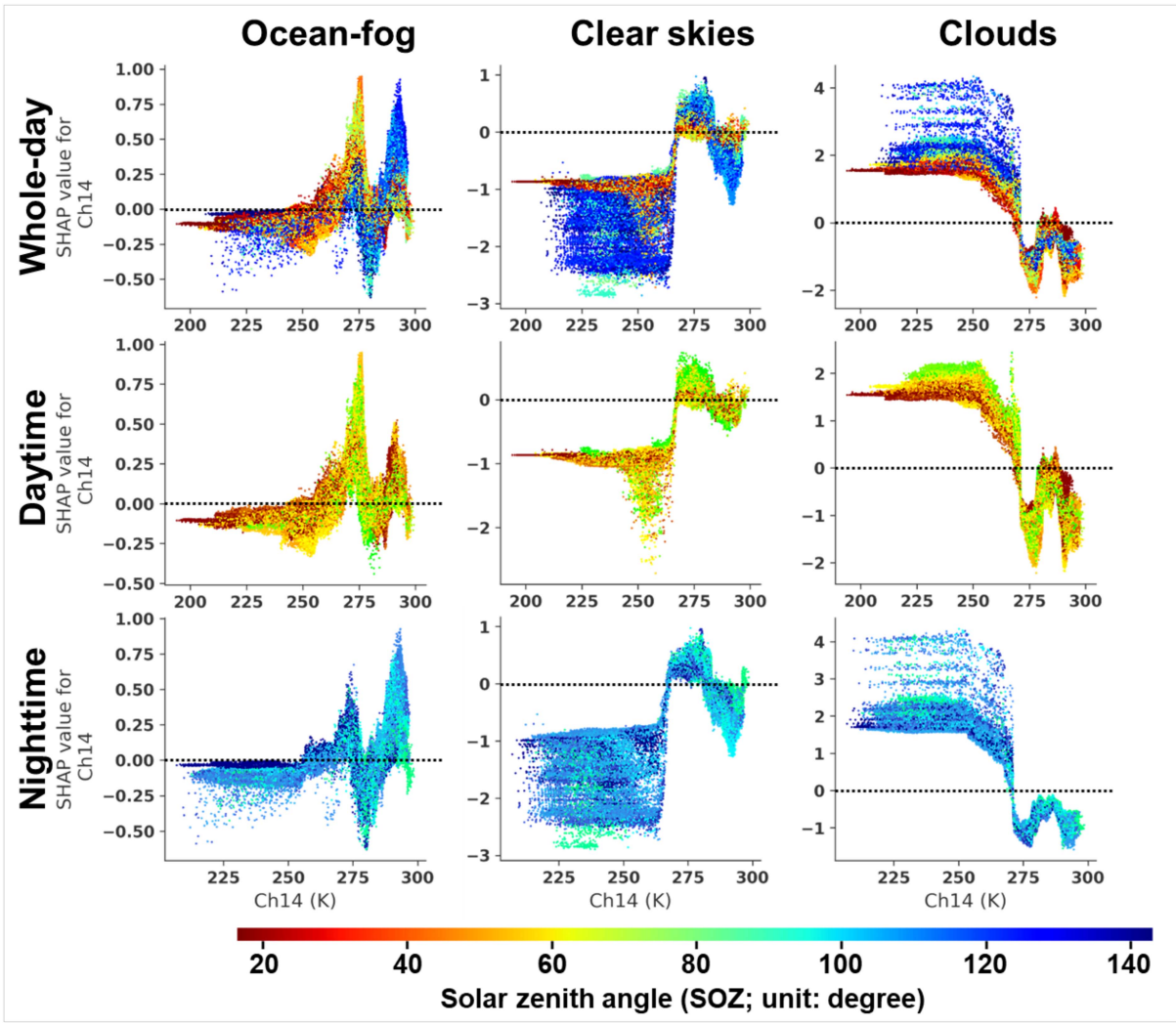

Fig. 7. Dependency plots of Ch14 by the solar zenith angle on extreme gradient boosting of infrared only used scheme in each temporal period. *X*-axis indicates values of input variables, the *y*-axis indicates SHAP values, and the color indicates the solar zenith angle.

positive contribution range of ocean–fog overlapped with the negative contribution range of clear skies and clouds. As solar radiation is absent at night, the primary source of Ch07 is surface emissions; therefore, blocking surface emissions by ocean–fog or clouds is implied. Consequently, positive values close to 0 K and negative values of BTD1407 are generally related to ocean–fog, clear skies, and clouds, respectively, resulting in positive SHAP values. Like BTD1407, BTD1107 contributed positively to ocean–fog; however, its positive contribution to clouds was more difficult to separate from ocean–fog, resulting in a lower contribution rank than BTD1407. Because Ch11 and Ch14 are both atmospheric window channels, ice crystals in clouds absorb more radiation at longer wavelengths [35]; consequently, the BT difference between ice-phase clouds and water-phase ocean–fog is greater in Ch14 than in Ch11, resulting in a more distinguishable pattern of positive and negative SHAP contributions to clouds (see Figs. 4 and 5). The contribution of the SOZ to ocean–fog detection ranked third. The SOZ is expected to reveal temporal information regarding the diurnal cycles of radiation and reflection.

Ch15 contributed the most to detecting ocean–fog among the atmospheric window channels. Ch15 $>$ 280 K contributed to the detection of daytime ocean–fog with an SHAP of up to 1, whereas Ch15 $<$ 270 K contributed to the omission of nonfog throughout the day with an SHAP of down to -3 (see Fig. 6). Ch14, however, is regarded as a classic atmospheric window channel and is widely used to distinguish atmospheric phenomena. Still, it contributed the least (see Fig. 7). Although Ch14 indicated the top kinetic temperature of a feature, its diurnal variation (lower temperature during the daytime and higher temperature at night) resulted in multiple peaks of positive SHAP values (see Fig. 7) [64]. However, Ch15, with a longer wavelength than Ch14, loses its BT from water vapor, which has a diurnal cycle of atmospheric water vapor (lower density in daytime and higher density at night) [56], [57], [58], [59], [60], [61], [62], [63], [64], [65], [66], [67], resulting in the cancellation of both diurnal variations and stable thermal property of ocean–fog on Ch15 regardless of the time of day.

In addition to the atmospheric window channels, Ch07, ranked fifth, contributed to detecting ocean–fog. Because Ch07

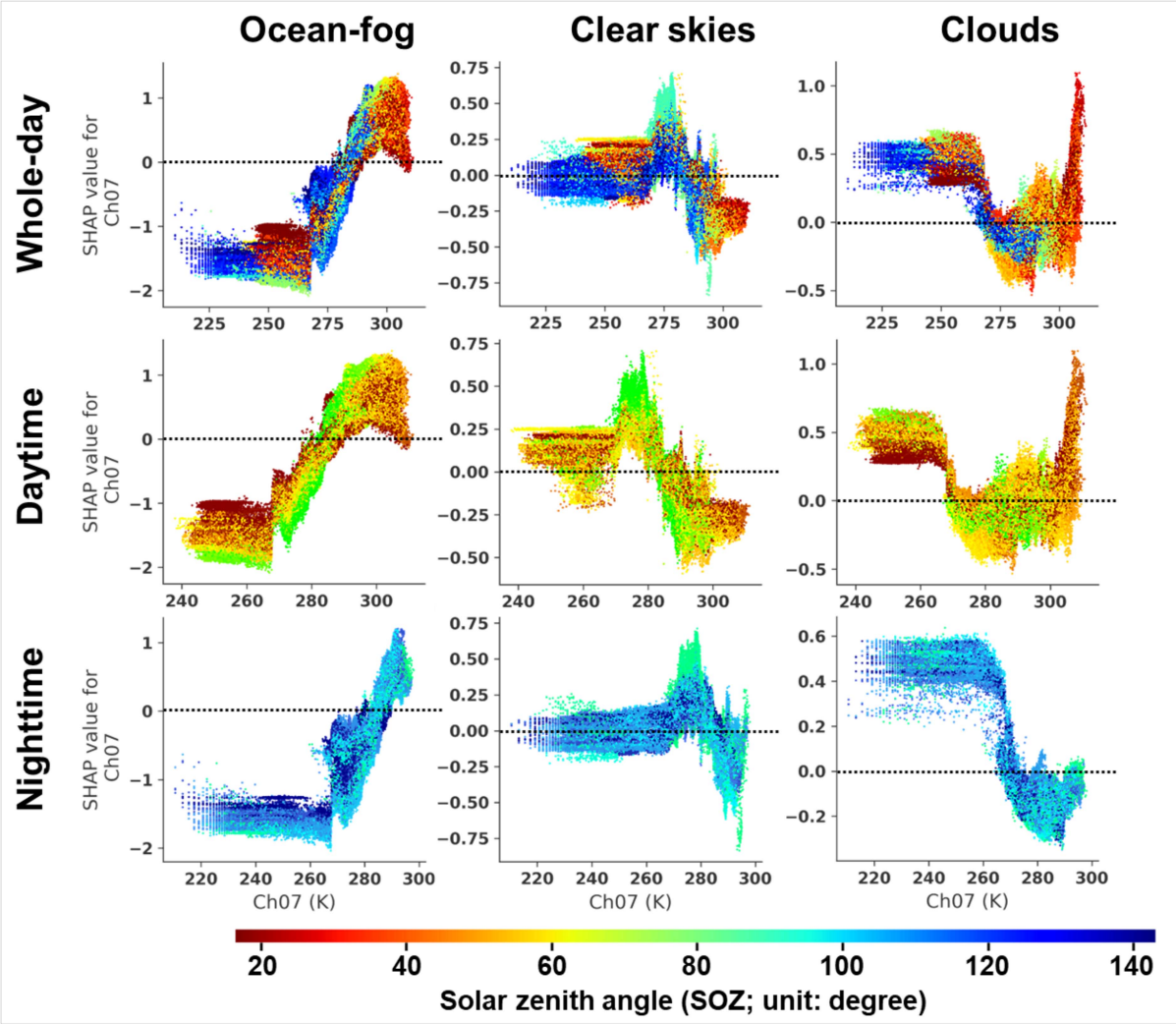

Fig. 8. Dependency plots of Ch07 by the solar zenith angle on extreme gradient boosting of infrared only used scheme in each temporal period. *X*-axis indicates values of input variables, the *y*-axis indicates SHAP values, and the color indicates the solar zenith angle.

reflects solar radiation during the daytime, high values of Ch07 greater than 290 K contributed to detecting ocean–fog (see Fig. 8). In contrast, low values of Ch07, less than 280 K, contributed to the omission of nonfog data. However, clouds also have high reflectance during the daytime; therefore, the positive contribution range is mixed with the negative contribution range, resulting in the worst variable contribution to cloud detection.

C. Spatiotemporal Distribution of Ocean–Fog

Fig. 9 shows ocean–fog detection maps along with Ch02 and Ch14 images at 14:40 KST on July 10, 2021, when CALIPSO detected ocean–fog. A large convective cloud with extremely high reflectance and a cold top temperature was found in region A's Ch02 and Ch14 images. Despite the solid formation of the convective cloud, weak Ch02 signals were detected in the peripheral regions of the cloud owing to the lower density of obstructions. Most edges were classified as ocean–fog in VIS_XGB, with Ch02 being the most influential variable, whereas IRO_XGB and NMSC classified clouds well.

A CALIPSO-based reference confirmed that Region B is primarily cloudy, with unknown ocean–fog conditions in the south. According to Ch02 and Ch14, stratus cumulus clouds with rough textures and high reflectance were suspected in B's northern and central regions; consequently, all models accounted for these regions as cloudy. However, NMSC missed all ocean–fog regions south of Region B, which the machine-learning models correctly classified. Even though ideal ocean–fog signals were detected in the south of region B, NMSC could classify them as clouds owing to the rough texture of the region, whereas machine-learning models, which do not utilize texture information, detect ocean–fog pixel-by-pixel correctly.

CALIPSO revealed that Region C consists of ocean–fog and clear skies in its one-dimensional data. This region was

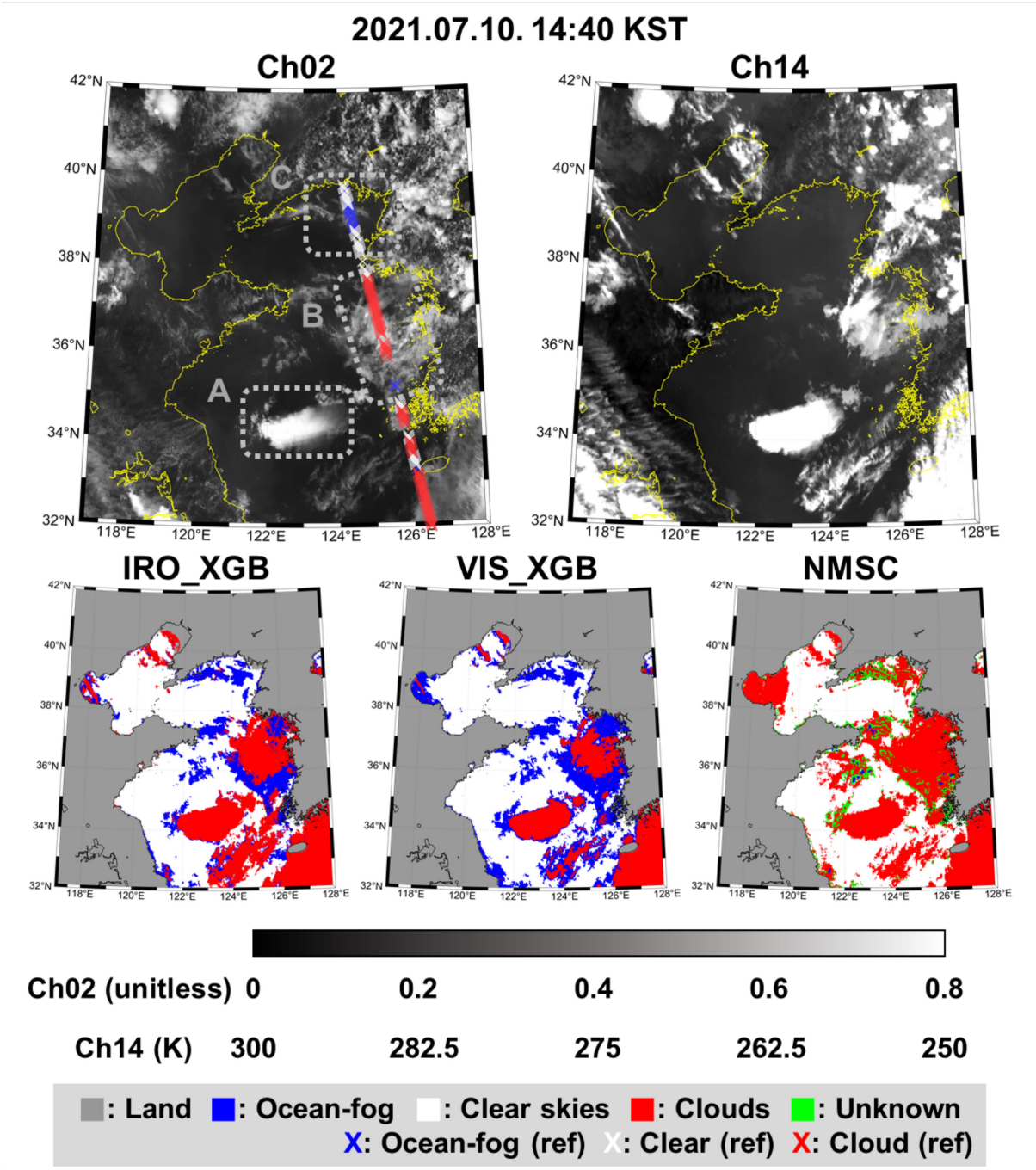

Fig. 9. Ocean–fog distribution maps of Ch02, Ch14, extreme gradient boosting using infrared only scheme (IRO_XGB), extreme gradient boosting with a visible channel (VIS_XGB), and product of NMSC at July 10, 2021, 14:40 KST. The scattered dots indicate ocean–fog reference from the CALIPSO.

uniformly warm with a mean Ch14 of 288 K and transparent with a mean Ch02 of 0.05. It was classified as a cloud by the NMSC algorithm, identifying pixels over a Ch02 of 0.26 as ocean–fog. Machine-learning models detected ocean–fog pixels perfectly in this region. In contrast, NMSC misclassified ocean–fog pixels and surrounding clear-sky pixels as clouds because of the rough texture information caused by sparse small ocean–fog pieces; this is an excessive misclassification compared to region A in which the ocean–fog and the surrounding clouds were classified as clouds.

Region C was further evaluated using the time-series results starting from 14:40 KST (i.e., the CALIPSO observation time) to 30 min later with 10-min intervals (see Fig. 10). During this time, the horizontal movement of obstacles (potential ocean–fog) was minimal. Still, transparency variation was present, resulting in a change in radiation on the ocean–fog edge regions. For example, at approximately 39°20'N, 124°E (yellow box region of Ch02 at 14:40 KST), IRO_XGB had confusion between ocean–fog and clouds, whereas VIS_XGB showed well-segmented ocean–fog consistently. In contrast, NMSC classifies this region as a

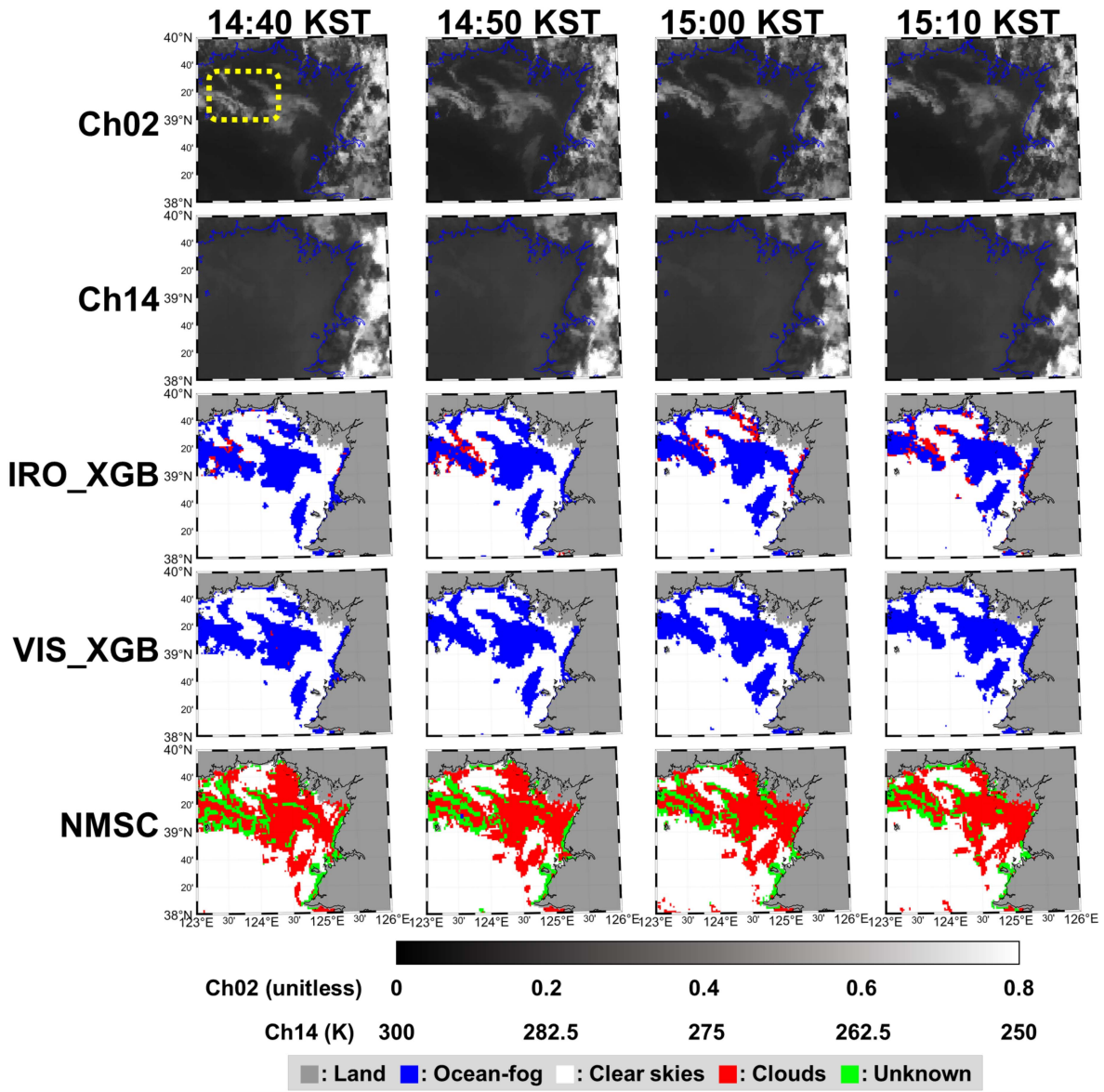

Fig. 10. Ocean-fog distribution maps of Ch02, Ch14, extreme gradient boosting using infrared only scheme (IRO_XGB), extreme gradient boosting with a visible channel (VIS_XGB), and product of NMSC over an area 38–40°N 123–126°E from July 10, 2021, 14:40 KST to 15:10 KST with a 10-min interval. The yellow box region of Ch02 at 14:40 KST demonstrates a temporally unstable transparency region.

blend of cloudy and unknown classes. Furthermore, because NMSC classifies ocean–fog as having a uniform texture, this area's uneven texture led to misclassification by NMSC as a cloud class.

The BN station also acquired reports of ocean–fog occurrences near this time; consequently, an hourly quantitative assessment was implemented using a window of 5 × 5 pixels surrounding the station (see Fig. 11). The ASOS station reports hourly. At 14:00 KST, BN reported a mist with 80% stratus cumulus (Sc) and cirrus (Ci) coverage. Although mist was reported, clouds covered approximately 80% of the sky. Consequently, IRO_XGB classified this instance as clouds with minor ocean–fog. VIS_XGB and NMSC also classified this region as clouds from 13:30 to 14:00 KST; however, after 14:00 KST, they classified it as ocean–fog or unknown classes, respectively. Finally, at 15:00 KST, a mist with 60% Ci clouds was observed at the station. Because Ci clouds only covered 60% of the sky, IRO_XGB and VIS_XGB classified this region as a mixture of ocean–fog and clear skies with Ci clouds. However, even though there was ocean–fog-like radiation, the texture of the region in the satellite images was rough owing to shallow ocean-fog (mist) and covering cirrus clouds, causing this region to appear as a mixture of unknown clear skies and clouds without ocean–fog.

From 16:30 to 18:30 KST, no ocean–fog was reported in this region; however, as of 18:30 KST, mist without cloud cover was reported at the station. The period around 17:00 KST was a day-to-night transition; the reflectances of Ch02 and Ch07 decreased to zero at night, and machine-learning models using the data may have produced unstable classification results.

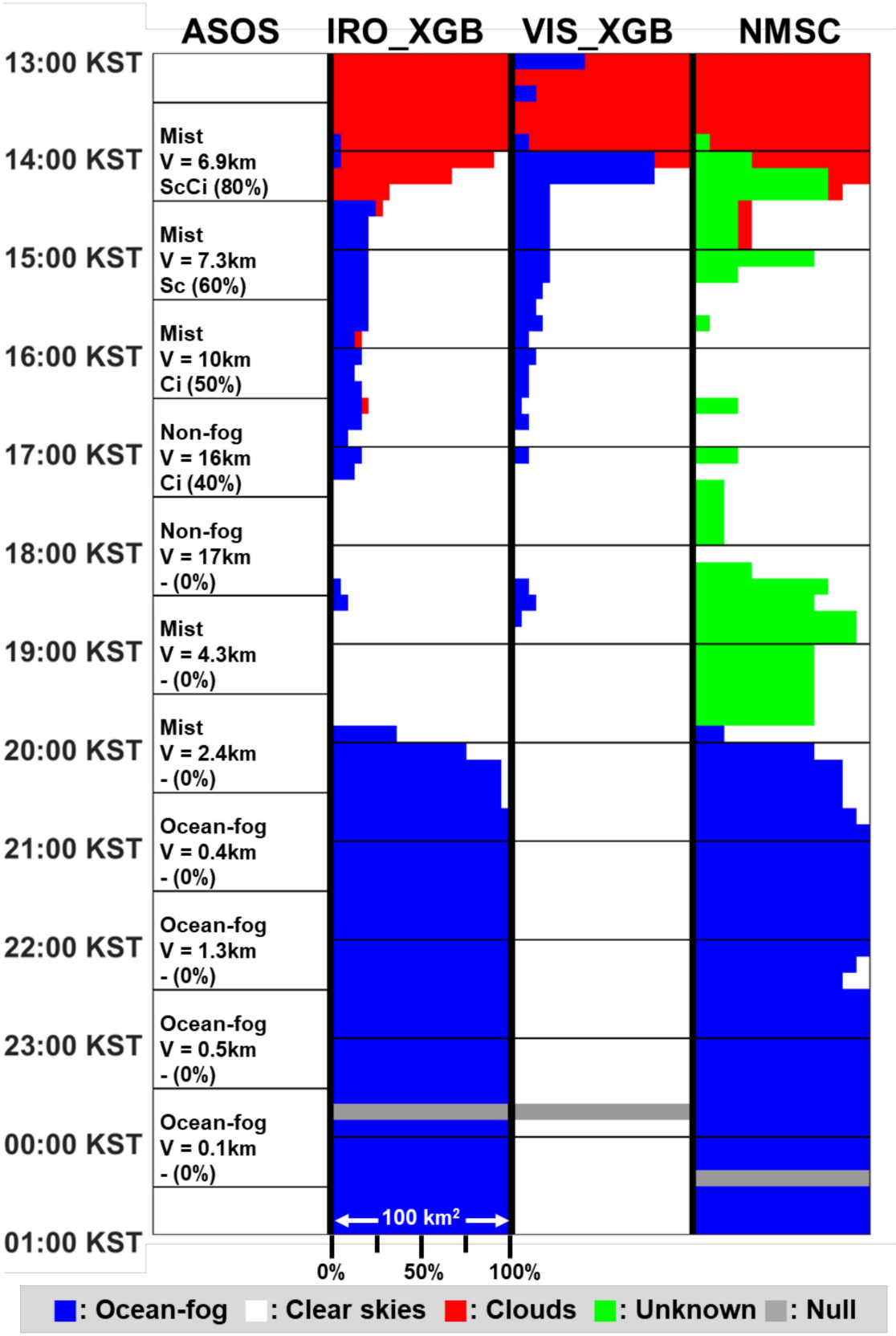

Fig. 11. Temporal reporting of weather, visibility, and cloud amount from the Baenyeongdo ASOS station, with the proportion of detection in the area of 100 km^2 (25 pixels) based on the extreme gradient boosting with the infrared only scheme (IRO_XGB), extreme gradient boosting with a visible channel scheme (VIS_XGB), and product of NMSC from July 10, 2021, 13:00 KST to July 11, 2021, 00:50 KST with a 10-min interval. V means visibility.

The NMSC results exhibited an abnormal increase in the high proportion of unknown classes in this region between 18:10 and 19:50 KST since the ocean–fog detection model was converted from a daytime model to a dawn/dusk model. BN reported mist without cloud cover at 20:00 KST and ocean–fog at 21:00 KST, resulting in a progressive increase in the ocean—fog fraction on IRO_XGB and NMSC from 19:50 KST, whereas VIS_XGB did not provide output at night. Ocean–fog, not mist, was detected at approximately 21:00 KST, and IRO_XGB and NMSC correctly identified it.

D. Novelty and Limitations

This article proposes a novel approach for ocean–fog detection using geostationary satellite data. This article had four major findings. First, the semiautomated sampling method proposed in this article generated many samples with high confidence. In contrast, previous articles collected all nearby pixels without QC or collocated them with human-inspected ocean–fog patches. Second, the model proposed in this article classifies three types of phenomena (ocean–fog, clear skies, and clouds) regardless of the time of day or night. Third, most previous articles, including NMSC, have focused on ocean–fog discrimination [13], [16]. Because the criteria distinguishing ocean–fog, clear sky, and cloud pixels vary with time and input variables, it is difficult for a model to classify ocean–fog and nonfog without causing confusion between ocean–fog and clear skies or clouds. However, this article modeled three marine atmospheric conditions as target classes, resulting in increased performance regardless of diurnal variation.

Third, this article attempted to interpret the results of a complex machine-learning model. Although some previous articles have conducted model interpretation, only a few well-known input variables or simple structured models (i.e., decision trees) have been used for simple interpretation, limiting the scientific findings [16], [18]. However, this article used the SHAP approach to interpret the results in detail, specifically how the change in input variables (i.e., BTD1107 and BTD1407) influenced the three-class classification, focusing on their temporal variation and how the use of Ch15 versus Ch14 was effective in detecting ocean–fog.

Fourth, the proposed model successfully detects ocean–fog using spectral rather than textural information. Previous ocean–fog detection models were built using simple thresholding or empirical modeling, incorporating spectral and texture information as input variables. However, texture information is only effective under ideal conditions (i.e., the interior of large ocean–fog without cloud contamination), resulting in misclassification over small or ocean–fog edge regions. In this article, a more advanced empirical modeling technique (i.e., XGB) was combined with spectral information to construct a model that can be used for ocean–fog detection under a variety of ocean–fog sizes and occurrences, resulting in reliable ocean–fog detection and even ocean–fog pixels in gaps between clouds or small sizes.

Nevertheless, this article has several limitations. First, ASOS and CALIPSO-derived ocean–fog cases were used as reference data, which were collected at specific locations (i.e., BN, HS, IC, and MP stations) or specific periods (i.e., around 5:00 or 17:00 KST for CALIPSO), thereby limiting the comprehensive spatiotemporal evaluation of the proposed model for ocean–fog. Second, even with spatial oversampling through K-means clustering to broaden the spatial coverage, it was impossible to cover the entire Yellow Sea every time, resulting in insufficient modeling generalization. Third, the main characteristics of ocean–fog are its high transparency and warm temperatures. However, the edges of stratus clouds generally have properties similar to ocean–fog, confusing the suggested model. Fourth, machine-learning models perform well in detecting ocean–fog cases similar to the training data; however, they can lead to misclassifications of ocean–fog cases with distinct spectral information. Although this article proposes a novel model for detecting ocean–fog, the reliability of ocean–fog detection results is compromised during the transition between day and night owing to the discontinuous spectral property of Ch07 in that period. Although SHAP provides insights into model interpretation through a statistical approach, it does not offer a complete understanding of the model structure and is, therefore, subject to potential errors.

V. Conclusion

While continuous and stable ocean–fog monitoring is necessary, previous articles have developed models capable of detecting ocean–fog during specific diurnal periods (e.g., day, night, and dawn/dusk). Therefore, this article proposes a model (IRO_XGB) for ocean–fog detection via the Himawari-8 satellite using machine-learning and an objective procedure, regardless of whether it is day or night. This model was evaluated by comparing it with NMSC, an operational product, and VIS_XGB, designed for daytime ocean–fog detection with visible and IR channels. IRO_XGB quantitatively classified all classes (i.e., ocean–fog, clear sky, and clouds) perfectly during the daytime, whereas VIS_XGB misclassified 4.76% of the cloud cases as ocean–fog, and NMSC omitted 10% of the ocean–fog cases. During the nighttime, IRO_XGB perfectly corrected ocean–fog, and only 5.56% of clear-sky cases were misclassified as ocean–fog, whereas NMSC omitted 14% of ocean–fog cases.

Consequently, in a whole-day view, IRO_XGB perfectly corrected ocean—fog with 4.05% false alarms from clear skies, while NMSC omitted 12.86% of the ocean–fog; this was also demonstrated in a spatial evaluation; for instance, IRO_XGB and NMSC classified convective clouds well, but NMSC classified mixed regions of ocean–fog and nonfog (i.e., clear sky and cloud) as clouds, whereas IRO_XGB classified these regions as mixtures referred to by the CALIPSO reference. In the temporal evaluation, IRO_XGB and NMSC stably detected persistent ocean–fog, but IRO_XGB produced more secure classification results over mists and clouds than NMSC. This article revealed, as a result of SHAP analysis, that the change in the BTD between channels 14 and 7 (BTD1407) was the most contributing variable and capability of Ch15. In contrast, the classical atmospheric

window channel, Ch14, was affected by the diurnal temperature cycle under marine atmospheric conditions. Although the suggested model utilized limited reference data, it exhibited high quantitative and qualitative performances. In the future, when diverse spatial and temporal references are gathered, a more general and high-performance model can be developed.

REFERENCES

[1] I. Gultepe, M. D. Müller, and Z. Boybeyi, "A new visibility parameterization for warm-fog applications in numerical weather prediction models," *J. Appl. Meteorol. Climatol.*, vol. 45, no. 11, pp. 1469–1480, 2006, doi: 10.1175/JAM2423.1.

[2] X. Wu and S. Li, "Automatic sea fog detection over Chinese adjacent oceans using Terra/MODIS data," *Int. J. Remote Sens.*, vol. 35, no. 21, pp. 7430–7457, 2014, doi: 10.1080/01431161.2014.968685.

[3] D. Wu, B. Lu, T. Zhang, and F. Yan, "A method of detecting sea fogs using CALIOP data and its application to improve MODIS-based sea fog detection," *J. Quantitative Spectrosc. Radiative Transfer*, vol. 153, pp. 88–94, 2015, doi: 10.1016/j.jqsrt.2014.09.021.

[4] *World Meteorological Organization, Guide to Meteorological Instruments and Methods of Observation*, World Meteorological Organization, Geneva, Switzerland, 2017, doi: 10.25607/OBP-432.

[5] V. Bertram, *Practical Ship Hydrodynamics*. Amsterdam, The Netherlands: Elsevier, 2012.

[6] A. C. W. Leung, W. A. Gough, and K. A. Butler, "Changes in fog, ice fog, and low visibility in the Hudson bay region: Impacts on aviation," *Atmosphere*, vol. 11, no. 2, pp. 1–19, 2020, doi: 10.3390/atmos11020186.

[7] K. Heo, S. Park, K. Ha, and J. Shim, "Algorithm for sea fog monitoring with the use of information technologies," *Meteorol. Appl.*, vol. 14, no. 2, pp. 117–129, 2014, doi: 10.1002/met.13.

[8] Y. Choi, H. G. Choe, J. Y. Choi, K. T. Kim, J. B. Kim, and N. Il Kim, "Automatic sea fog detection and estimation of visibility distance on CCTV," *J. Coastal Res.*, vol. 85, no. 85, pp. 881–885, 2018, doi: 10.2112/SI85-177.1.

[9] T. W. Bae, J. H. Han, K. J. Kim, and Y. T. Kim, "Coastal visibility distance estimation using dark channel prior and distance map under sea-fog: Korean Peninsula case," *Sensors*, vol. 19, no. 20, 2019, Art. no. 4432, doi: 10.3390/s19204432.

[10] Marine weather information portal. [Internet]. (cited 2023, June 6), Korea Meteorological Administration (KMA). [Online]. Available: https://marine.kma.go.kr/mmis/

[11] C. Lin, Z. Zhang, Z. Pu, and F. Wang, "Numerical simulations of an advection fog event over Shanghai Pudong International Airport with the WRF model," *J. Meteorol. Res.*, vol. 31, no. 5, pp. 874–889, 2017, doi: 10.1007/s13351-017-6187-2.

[12] D. H. Richter, T. MacMillan, and C. Wainwright, "A Lagrangian cloud model for the study of marine fog," *Boundary-Layer Meteorol.*, vol. 181, no. 2–3, pp. 523–542, 2021, doi: 10.1007/s10546-020-00595-w.

[13] M. S. Suh, J. H. Han, N. Y. Noh, and H. Y. Yoo, "Algorithm theoretical basis document: Fog," National Meteorological Satellite Center, Korea, 2019. [Online]. Available: https://nmsc.kma.go.kr/homepage/html/base/cmm/selectPage.do?page=static.edu.atbdGk2a

[14] H. S. Ryu and S. Hong, "Sea fog detection based on normalized difference snow index using advanced Himawari imager observations," *Remote Sens.*, vol. 12, no. 9, 2020, Art. no. 1521, doi: 10.3390/RS12091521.

[15] J. Zhu et al., "Demonstration of measuring sea fog with an SNSPD-based lidar system," *Sci. Rep.*, vol. 7, no. 1, pp. 1–7, 2017, doi: 10.1038/s41598-017-15429-y.

[16] D. Kim, M.-S. Park, Y.-J. Park, and W. Kim, "Geostationary ocean color imager (GOCI) marine fog detection in combination with Himawari-8 based on the decision tree," *Remote Sens.*, vol. 12, no. 1, 2020, Art. no. 149, doi: 10.3390/rs12010149.

[17] M. Amani, S. Mahdavi, T. Bullock, and S. Beale, "Automatic nighttime sea fog detection using GOES-16 imagery," *Atmos. Res.*, vol. 238, 2020, Art. no. 104712, doi: 10.1016/j.atmosres.2019.104712.

[18] S. Mahdavi, M. Amani, T. Bullock, and S. Beale, "A probability-based daytime algorithm for sea fog detection using GOES-16 imagery," *IEEE J. Sel. Topics Appl. Earth Observ. Remote Sens.*, vol. 14, pp. 1363–1373, Nov. 2021, doi: 10.1109/JSTARS.2020.3036815.

[19] D. Shin and J. H. Kim, "A new application of unsupervised learning to nighttime sea fog detection," *Asia-Pacific J. Atmos. Sci.*, vol. 54, no. 4, pp. 527–544, 2018, doi: 10.1007/s13143-018-0050-y.

[20] S. H. Kim, M. S. Suh, and J. H. Han, "Development of fog detection algorithm during nighttime using Himawari-8/AHI satellite and ground observation data," *Asia-Pacific J. Atmos. Sci.*, vol. 55, no. 3, pp. 337–350, 2019, doi: 10.1007/s13143-018-0093-0.

[21] M. Kim, J. Im, H. Park, S. Park, M. I. Lee, and M. H. Ahn, "Detection of tropical overshooting cloud tops using Himawari-8 imagery," *Remote Sens.*, vol. 9, no. 7, pp. 1–19, 2017, doi: 10.3390/rs9070685.

[22] M. Kim, J. Lee, and J. Im, "Deep learning-based monitoring of overshooting cloud tops from geostationary satellite data," *GISci. Remote Sens.*, vol. 55, no. 5, pp. 763–792, 2018, doi: 10.1080/15481603.2018.1457201.

[23] S. Sim, J. Im, S. Park, H. Park, M. H. Ahn, and P. wai Chan, "Icing detection over East Asia from geostationary satellite data using machine learning approaches," *Remote Sens.*, vol. 10, no. 4, 2018, Art. no. 631, doi: 10.3390/rs10040631.

[24] D. Han, J. Lee, J. Im, S. Sim, S. Lee, and H. Han, "A novel framework of detecting convective initiation combining automated sampling, machine learning, and repeated model tuning from geostationary satellite data," *Remote Sens.*, vol. 11, no. 12, 2019, Art. no. 1454, doi: 10.3390/rs11121454.

[25] J. Lee, M. Kim, J. Im, H. Han, and D. Han, "Pre-trained feature aggregated deep learning-based monitoring of overshooting tops using multi-spectral channels of GeoKompsat-2A advanced meteorological imagery," *GISci. Remote Sens.*, vol. 58, no. 7, pp. 1052–1071, 2021, doi: 10.1080/15481603.2021.1960075.

[26] D. Han, M. Choo, J. Im, Y. Shin, J. Lee, and S. Jung, "Precipitation nowcasting using ground radar data and simpler yet better video prediction deep learning," *GISci. Remote Sens.*, vol. 60, no. 1, 2023, Art. no. 2203363, doi: 10.1080/15481603.2023.2203363.

[27] X. Lü, F. Qiao, C. Xia, G. Wang, and Y. Yuan, "Upwelling and surface cold patches in the Yellow Sea in summer: Effects of tidal mixing on the vertical circulation," *Continental Shelf Res.*, vol. 30, no. 6, pp. 620–632, 2010, doi: 10.1016/j.csr.2009.09.002.

[28] J. Lee, I.-C. Pang, and J.-H. Moon, "Contribution of the Yellow Sea bottom cold water to the abnormal cooling of sea surface temperature in the summer of 2011," *J. Geophys. Res. Ocean.*, vol. 121, pp. 3372–3380, 2016, doi: 10.1002/2016JC011658.

[29] K. Heo and K. Ha, "Classification of synoptic pattern associated with coastal fog around the Korean peninsula," *Korean J. Atmos. Sci.*, vol. 40, no. 5, pp. 541–556, 2004.

[30] J. Brunner, R. B. Pierce, and A. Lenzen, "Development and validation of satellite-based estimates of surface visibility," *Atmos. Meas. Tech.*, vol. 9, no. 2, pp. 409–422, 2016, doi: 10.5194/amt-9-409-2016.

[31] S. Lee and J. Choi, "A snow cover mapping algorithm based on a multitemporal dataset for GK-2A imagery," *GISci. Remote Sens.*, vol. 59, no. 1, pp. 1078–1102, 2022, doi: 10.1080/15481603.2022.2097395.

[32] H. Lee and M. Suh, "Objective classification of fog type and analysis of fog characteristics using visibility meter and satellite observation data over South Korea," *Atmos. Korean Meteorol. Soc.*, vol. 29, no. 5, pp. 639–658, 2019.

[33] D. M. Winker and J. Pelon, "The CALIPSO mission: A global 3D view of aerosols and clouds," *Bull. Amer. Meteorol. Soc.*, vol. 91, no. 9, pp. 1211–1230, 2010, doi: 10.1175/2010bams3009.1.

[34] K. Bessho et al., "An introduction to Himawari-8/9—Japan's new-generation geostationary meteorological satellites," *J. Meteorol. Soc. Jpn.*, vol. 94, no. 2, pp. 151–183, 2016, doi: 10.2151/jmsj.2016-009.

[35] M. J. Pavolonis, "GOES-R advanced baseline imager (ABI) algorithm theoretical basis document for cloud type and cloud phase," NPCA. NESDIS/STAR Algorithm Theoretical Basis Doc., version 2.0, 2010.

[36] T. J. Schmit, S. S. Lindstrom, J. J. Gerth, and M. M. Gunshor, "Applications of the 16 spectral bands on the Advanced Baseline Imager (ABI)," *J. Oper. Meteorol.*, vol. 6, no. 4, pp. 33–46, 2018, doi: 10.15191/nwajom.2018.0604.

[37] A. K. Heidinger et al., "ABI cloud products from the GOES-R series," in *The GOES-R Series*. Amsterdam, The Netherlands: Elsevier, 2020, pp. 43–62.

[38] D. T. Lindsey, L. Grasso, J. F. Dostalek, and J. Kerkmann, "Use of the GOES-R split-window difference to diagnose deepening low-level water vapor," *J. Appl. Meteorol. Climatol.*, vol. 53, no. 8, pp. 2005–2016, 2014, doi: 10.1175/JAMC-D-14-0010.1.

[39] F. Mokdad and B. Haddad, "Improved infrared precipitation estimation approaches based on k-means clustering: Application to north Algeria using MSG-SEVIRI satellite data," *Adv. Space Res.*, vol. 59, no. 12, pp. 2880–2900, 2017, doi: 10.1016/j.asr.2017.03.027.

[40] G. Devika and S. Parthasarathy, "Fuzzy statistics-based affinity propagation technique for clustering in satellite cloud image," *Eur. J. Remote Sens.*, vol. 51, no. 1, pp. 754–764, 2018, doi: 10.1080/22797254.2018.1482731.

[41] Z. Wang, J. R. Jensen, and J. Im, "An automatic region-based image segmentation algorithm for remote sensing applications," *Environ. Model. Softw.*, vol. 25, no. 10, pp. 1149–1165, 2010, doi: 10.1016/j.envsoft.2010.03.019.
[42] Z. Chang et al., "Landslide susceptibility prediction based on remote sensing images and GIS: Comparisons of supervised and unsupervised machine learning models," *Remote Sens.*, vol. 12, no. 3, 2020, Art. no. 502, doi: 10.3390/rs12030502.
[43] B. Basu, S. Sannigrahi, A. S. Basu, and F. Pilla, "Development of novel classification algorithms for detection of floating plastic debris in coastal waterbodies using multispectral Sentinel-2 remote sensing imagery," *Remote Sens.*, vol. 13, no. 8, 2021, Art. no. 1598, doi: 10.3390/rs13081598.
[44] J. A. Hartigan and M. A. Wong, "Algorithm AS 136: A K-means clustering algorithm," *J. Roy. Statist. Soc. Ser. C (Appl. Statist.)*, vol. 28, no. 1, pp. 100–108, 1979.
[45] A. Likas, N. Vlassis, and J. J. Verbeek, "The global k-means clustering algorithm," *Pattern Recognit.*, vol. 36, no. 2, pp. 451–461, 2003, doi: 10.1016/S0031-3203(02)00060-2.
[46] B. B. Mandelbrot, *The Fractal Geometry of Nature*, vol. 1. San Francisco, CA, USA: Freeman, 1982.
[47] K. McGarigal, *FRAGSTATS: Spatial Pattern Analysis Program for Quantifying Landscape Structure*, vol. 351. U.S. Department of Agriculture, Forest Service, Pacific Northwest Research Station, 1995.
[48] K. McGarigal, *FRAGSTATS Help*. Amherst, MA, USA: Univ. Massachusetts, 2015, Art. no. 182.
[49] M. R. Mireles, K. L. Pederson, and C. H. Elford, *Meteorologial Techniques (Revision 21 Feb 2007)*. AIR FORCE WEATHER AGENCY OFFUTT AFB NE, 2003.
[50] B. Purbantoro et al., "Comparison of aqua/terra MODIS and Himawari-8 satellite data on cloud mask and cloud type classification using split window algorithm," *Remote Sens.*, vol. 11, no. 24, pp. 1–19, 2019, doi: 10.3390/rs11242944.
[51] L. Breiman, "Random forests," *Mach. Learn.*, vol. 45, no. 1, pp. 5–32, 2001.
[52] D. W. Hosmer Jr, S. Lemeshow, and R. X. Sturdivant, *Applied Logistic Regression*, vol. 398. Hoboken, NJ, USA: Wiley, 2013.
[53] T. Chen and C. Guestrin, "XGBoost: A scalable tree boosting system," in *Proc. ACM SIGKDD Int. Conf. Knowl. Discov. Data Mining*, 2016, pp. 785–794, doi: 10.1145/2939672.2939785.
[54] M. Mahoney, L. Johnson, E. Bevilacqua, and C. Beier, "Filtering ground noise from LiDAR returns produces inferior models of forest aboveground biomass in heterogenous landscapes," *GISci. Remote Sens.*, vol. 59, no. 1, pp. 1266–1280, 2022, doi: 10.1080/15481603.2022.2103069.
[55] Y. Kang, E. Jang, J. Im, and C. Kwon, "A deep learning model using geostationary satellite data for forest fire detection with reduced detection latency," *GISci. Remote Sens.*, vol. 59, no. 1, pp. 2019–2035, 2022, doi: 10.1080/15481603.2020.2143872.
[56] J. E. King, "Binary logistic regression," in *Best Pract. Quantitative Methods*, Thousand Oaks, CA: Sage Publications, 2008, pp. 358–384. [Online]. Available: https://doi.org/10.4135/9781412995627
[57] F. Pedregosa, G. Varoquaux, A. Gramfort, V. Michel, and B. Thirion, "Scikit-learn: Machine learning in python," *J. Mach. Learn. Res.*, vol. 12, pp. 2825–2830, 2011, doi: 10.1289/EHP4713.
[58] A. E. Maxwell and T. A. Warner, "Thematic classification accuracy assessment with inherently uncertain boundaries: An argument for center-weighted accuracy assessment metrics," *Remote Sens.*, vol. 12, no. 12, 2020, Art. no. 1905, doi: 10.3390/rs12121905.
[59] A. M. Abdi, "Land cover and land use classification performance of machine learning algorithms in a boreal landscape using Sentinel-2 data," *GISci. Remote Sens.*, vol. 57, no. 1, pp. 1–20, 2020, doi: 10.1080/15481603.2019.1650447.
[60] L. S. Shapley, *17. A Value for N-Person Games*. Princeton, NJ, USA: Princeton Univ. Press, 2016, pp. 307–318.
[61] J. Gao, Q. Meng, L. Zhang, and D. Hu, "How does the ambient environment respond to the industrial heat island effects? An innovative and comprehensive methodological paradigm for quantifying the varied cooling effects of different landscapes," *GISci. Remote Sens.*, vol. 59, no. 1, pp. 1643–1659, 2022, doi: 10.1080/15481603.2022.2127463.
[62] W. Zhang et al., "Can gross primary productivity products be effectively evaluated in regions with few observation data?," *GISci. Remote Sens.*, vol. 60, no. 1, 2023, Art. no. 2213489, doi: 10.1080/15481603.2023.2213489.
[63] J. V. Tu, "Advantages and disadvantages of using artificial neural networks versus logistic regression for predicting medical outcomes," *J. Clin. Epidemiol.*, vol. 49, no. 11, pp. 1225–1231, 1996, doi: 10.1016/S0895-4356(96)00002-9.
[64] S. Taylor, P. Stier, B. White, S. Finkensieper, and M. Stengel, "Evaluating the diurnal cycle in cloud top temperature from SEVIRI," *Atmos. Chem. Phys.*, vol. 17, no. 11, pp. 7035–7053, 2017, doi: 10.5194/acp-17-7035-2017.
[65] K. Hocke, F. Navas-Guzmán, L. Moreira, L. Bernet, and C. Mätzler, "Diurnal cycle in atmospheric water over Switzerland," *Remote Sens.*, vol. 9, no. 9, pp. 1–16, 2017, doi: 10.3390/rs9090909.
[66] S. Steinke, S. Wahl, and S. Crewell, "Benefit of high resolution COSMO reanalysis: The diurnal cycle of column-integrated water vapor over Germany," *Meteorol. Zeitschrift*, vol. 28, no. 2, pp. 165–177, 2019, doi: 10.1127/metz/2019/0936.
[67] S. Ziskin Ziv, Y. Yair, P. Alpert, L. Uzan, and Y. Reuveni, "The diurnal variability of precipitable water vapor derived from GPS tropospheric path delays over the Eastern Mediterranean," *Atmos. Res.*, vol. 249, 2021, Art. no. 105307, doi: 10.1016/j.atmosres.2020.105307.

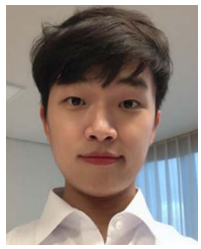

Seongmun Sim received the B.S. degree in environmental analysis & pollution control and the earth science & engineering from the Ulsan National Institute of Science and Technology (UNIST), Ulsan, South Korea, in 2015. He is currently working toward the doctoral degree in ocean fog detection/prediction using remote sensing and numerical predicted data with artificial intelligence techniques with the School of Urban and Environmental Engineering, UNIST.

His research interests include monitoring of oceanic and atmospheric phenomena using remote sensing and artificial intelligence.

Jungho Im (Member, IEEE) received the B.S. degree in oceanography and the M.C.P. degree in environmental studies from the Seoul National University, Seoul, South Korea, in 1998 and 2000, respectively, and the Ph.D. degree in remote sensing and GIS from the University of South Carolina, Columbia, SC, USA, in 2006.

He was with the SUNY-ESF, Syracuse, NY, USA, between 2007 and 2012, serving as an Assistant Professor. From 2012 to 2014, he was an Assistant Professor with the Ulsan National Institute of Science and Technology, Ulsan, South Korea, where he was an Associate Professor from 2014 to 2019, and has been a Full Professor, since 2019. His research interests include broadening and deepening of our understanding of the Earth systems on which society depends using remote sensing and artificial intelligence, and leverage this knowledge to better manage and control critical functions related to urban ecology, terrestrial, and coastal ecosystems, water resources, natural and man-made disasters, and carbon cycles.

Dr. Im has been serving as an Editor-in-Chief of GIScience and Remote Sensing since 2014 and an Associate Editor of ISPRS Journal of Photogrammetry and Remote Sensing since 2020.